

ART² : Coupling Ly α Line and Multi-wavelength Continuum Radiative Transfer

Hideobu Yajima^{1,2*}, Yuexing Li^{1,2}, Qirong Zhu^{1,2}, Tom Abel³

¹*Department of Astronomy and Astrophysics, Pennsylvania State University, 525 Davey Lab, University Park, PA 16802, USA*

²*Institute for Gravitation and the Cosmos, The Pennsylvania State University, University Park, PA 16802*

³*Kavli Institute for Particle Astrophysics and Cosmology, SLAC National Accelerator Laboratory, Stanford University, 2575 Sand Hill Road, Menlo Park, CA 94025, USA*

Accepted ??; Received ??; in original form ???

ABSTRACT

Narrow-band Ly α line and broad-band continuum have played important roles in the discovery of high-redshift galaxies in recent years. Hence, it is crucial to study the radiative transfer of both Ly α and continuum photons in the context of galaxy formation and evolution in order to understand the nature of distant galaxies. Here, we present a three-dimensional Monte Carlo radiative transfer code, All-wavelength Radiative Transfer with Adaptive Refinement Tree (ART²), which couples Ly α line and multi-wavelength continuum, for the study of panchromatic properties of galaxies and interstellar medium. This code is based on the original version of Li et al., and features three essential modules: continuum emission from X-ray to radio, Ly α emission from both recombination and collisional excitation, and ionization of neutral hydrogen. The coupling of these three modules, together with an adaptive refinement grid, enables a self-consistent and accurate calculation of the Ly α properties, which depend strongly on the UV continuum, ionization structure, and dust content of the object. Moreover, it efficiently produces multi-wavelength properties, such as the spectral energy distribution and images, for direct comparison with multi-band observations.

As an example, we apply ART² to a cosmological simulation that includes both star formation and black hole growth, and study in detail a sample of massive galaxies at redshifts $z = 3.1 - 10.2$. We find that these galaxies are Ly α emitters (LAEs), whose Ly α emission traces the dense gas region, and that their Ly α lines show a shape characteristic of gas inflow. Furthermore, the Ly α properties, including photon escape fraction, emergent luminosity, and equivalent width, change with time and environment. Our results suggest that LAEs evolve with redshift, and that early LAEs such as the most distant one detected at $z \sim 8.6$ may be dwarf galaxies with a high star formation rate fueled by infall of cold gas, and a low Ly α escape fraction.

Key words: radiative transfer – line: profiles – ISM: dust, extinction – galaxies: evolution – galaxies: formation – galaxies: high-redshift

1 INTRODUCTION

The hydrogen Ly α emission is one of the strongest lines in the UV band. It provides a unique and powerful tool to search for distant galaxies, as first suggested by Partridge & Peebles (1967), and evidenced by the successful detection of hundreds of Ly α emitting galaxies, or Ly α emitters (LAEs), at redshifts $z > 3$ over the past decade (e.g., Hu & McMahon 1996; Cowie & Hu

1998; Hu, Cowie, & McMahon 1998; Steidel et al. 2000; Rhoads et al. 2000; Fynbo, Möller, & Thomsen 2001; Hu et al. 2002; Fynbo et al. 2003; Rhoads et al. 2003; Ouchi et al. 2003; Kodaira et al. 2003; Maier et al. 2003; Hu et al. 2004; Dawson et al. 2004; Malhotra & Rhoads 2004; Horton et al. 2004; Taniguchi et al. 2005; Stern et al. 2005; Kashikawa et al. 2006; Shimasaku et al. 2006; Iye et al. 2006; Hu & Cowie 2006; Gronwall et al. 2007; Cuby et al. 2007; Stark et al. 2007; Nilsson et al. 2007; Ouchi et al. 2008; Willis, Courbin, Kneib, & Minniti 2008; Ota et al. 2008; Hu et al. 2010; Ouchi et al. 2010). More

* E-mail: yuh19@psu.edu(HY);

recently, Lehnert et al. (2010) have discovered the most distant galaxy at $z = 8.6$ using the Ly α line.

To obtain a full picture of the physical properties of the high-redshift LAEs, efforts have been made recently to observe these objects in broad-band continuum (e.g., Gawiser et al. 2006; Gronwall et al. 2007; Lai et al. 2007; Nilsson et al. 2007; Pirzkal et al. 2007; Lai et al. 2008; Ouchi et al. 2008; Pentericci et al. 2009; Ono et al. 2010a,b; Hayes et al. 2010; Finkelstein et al. 2011; Nilsson & Møller 2011). One remarkable result from these multi-wavelength surveys is that, LAEs appear to evolve with cosmic time: the LAEs at high redshifts $z > 5$ tend to be smaller and younger galaxies, and have less dust extinction and higher equivalent widths (EWs) than their counterparts at lower redshifts $z \sim 3$.

Despite the rapid progress in the Ly α detections, the origin and nature of these distant LAEs, however, remain largely unknown, because the radiative transfer (RT) of Ly α line is a complicated process. It depends on the geometry, kinematics, ionization state, and dust content of the surrounding medium, as well as the stellar population and other ionizing sources of the galaxy. To date, there have been a number of theoretical studies on the resonant scattering of Ly α photons, analytically in simple geometry (e.g., Hummer 1962; Adams 1972; Harrington 1973, 1974; Neufeld 1990, 1991; Loeb & Rybicki 1999), and numerically (e.g., Auer 1968; Avery & House 1968; Ahn, Lee, & Lee 2000, 2001, 2002; Zheng & Miralda-Escudé 2002; Dijkstra, Haiman, & Spaans 2006; Hansen & Oh 2006; Tasitsiomi 2006; Verhamme, Schaerer, & Maselli 2006; Laursen & Sommer-Larsen 2007; Laursen, Razoumov, & Sommer-Larsen 2009a; Pierleoni, Maselli, & Ciardi 2009; Faucher-Giguère et al. 2010; Zheng et al. 2010, 2011; Schaerer et al. 2011). Among the numerical codes, Monte Carlo method is widely employed to solve the Ly α RT, owing to the irregular geometry and inhomogeneous distribution of the interstellar medium (ISM), and the slow convergence of the numerical techniques at high optical depths. By applying Ly α RT codes to cosmological simulations, several aspects of the LAEs have been investigated by various groups, including observed properties of LAEs at $z \sim 5.7$ (Zheng et al. 2010, 2011), escape fraction of Ly α photons from high- z galaxies (Laursen, Sommer-Larsen, & Andersen 2009b), effects of ionization on the emergent Ly α spectra (Pierleoni et al. 2009), and mechanism of high EWs in dusty multi-phase ISM (Hansen & Oh 2006). However, most of these previous works have focused only on the Ly α line, and were therefore limited to some aspect of the Ly α properties, such as flux and line profile.

On the other hand, there has been an array of RT codes in continuum over the last several decades, using either ray-tracing methods (e.g., Rowan-Robinson 1980; Efstathiou & Rowan-Robinson 1990; Steinacker et al. 2003; Folini et al. 2003; Steinacker, Bacmann, & Henning 2006), or Monte Carlo methods (e.g., Witt 1977; Lefevre, Bergeat, & Daniel 1982; Lefevre, Daniel, & Bergeat 1983; Whitney & Hartmann 1992; Witt, Thronson, & Capuano 1992; Code & Whitney 1995; Lopez, Mekarnia, & Lefevre 1995; Lucy 1999; Wolf, Henning, & Stecklum 1999; Bianchi, Davies, & Alton 2000; Bjorkman & Wood 2001; Whitney et al. 2003;

Harries et al. 2004; Jonsson 2006; Pinte et al. 2006; Li et al. 2008; Chakrabarti & Whitney 2009). In particular, Li et al. (2008) developed a multi-wavelength RT code that employs radiative equilibrium and an adaptive refinement grid, which reproduced the observed dust properties of the most distant quasars detected at $z \sim 6$ when applied to the hydrodynamic quasar simulations of Li et al. (2007).

However, most of these developments focused mainly on radiation transport in dusty environments, in particular the absorption and re-emission by dust, of local star-forming regions. In order to explain the diverse properties of LAEs and their evolution with redshift, it is critical to couple Ly α with continuum, in the context of galaxy formation and evolution. Several aspects of such an approach have been attempted in previous studies. For examples, Pierleoni et al. (2009) incorporated pre-computed grid of Ly α RT into ionization calculations, Tasitsiomi (2006) considered a combination of Ly α and ionization RT, Laursen, Sommer-Larsen, & Andersen (2009b) studied the effect of ionization and dust on transfer of Ly α photons, while Schaerer et al. (2011) included dust and non-ionizing UV continuum in the Ly α RT calculations. An ultimate goal would be to tackle the ionization of hydrogen, non-ionizing continuum, interstellar dust, and Ly α propagation and scattering simultaneously.

Furthermore, the implementation of Ly α emission should include two major generation mechanisms, the recombination of ionizing photons, and collisional excitation of hydrogen gas. In addition, relevant ionizing sources such as stars, active galactic nucleus (AGN), and UV background radiation should be included. Last, but not the least, the RT code should incorporate an adaptive refinement grid in order to cover a large dynamical range and resolve dense gas regions where star formation takes place and prominent Ly α emission comes from (Laursen et al. 2009a).

In this work, we present a new, 3-D Monte Carlo RT code, All-wavelength Radiative Transfer with Adaptive Refinement Tree (ART²), which couples Ly α line and multi-wavelength continuum, for the study of panchromatic properties of galaxies and ISM. (Note that the “coupling” in this paper means the RT of Ly α with other continuum photons, not the coupling between RT and hydrodynamics.) Our code improves over the original continuum-only version of Li et al. (2008), and features three essential modules: continuum emission from X-ray to radio, Ly α emission from both recombination and collisional excitation, and ionization of neutral hydrogen. The coupling of these three modules enables a self-consistent and accurate calculation of the Ly α and multi-wavelength properties of galaxies, as the equivalent width of the Ly α line depends on the UV continuum, and the escape fraction of Ly α photons strongly depends on the ionization structure and the dust content of the object. Moreover, the adaptive refinement grid handles arbitrary geometry and efficiently traces inhomogeneous density distribution in galaxies and ISM. Furthermore, this code takes into account radiation from both stars and accreting black holes, so it can be used to study both galaxies and AGNs. ART² can produce a number of observables, including spectral energy distribution (SED) from X-ray to radio, multi-band fluxes and images, Ly α emission line and its EW, which can be directly compared to real observations. It has a wide range of applications, and can be easily applied to simulations using either grid-based or smoothed particle hydrody-

namic (SPH) codes by converting the simulation snapshot to the grid structure of ART².

The paper is organized as follows. In §2, we describe the ART² code, which includes implementation of three modules of Continuum, Ly α line, and Ionization of hydrogen, the adaptive refinement grid, and the dust model. In §3, we present the application of ART² to a SPH cosmological simulation, and study in details the Ly α emission and multi-band properties from individual galaxies at redshifts $z=8.5$, 6.2, and 3.1 from the simulation. We discuss in §4 contribution to Ly α emission from AGNs, stars, and excitation cooling from gas accretion in our model, and effects of numerical resolutions on the RT calculations, and summarize in §5.

2 ART²: ALL-WAVELENGTH RADIATIVE TRANSFER WITH ADAPTIVE REFINEMENT TREE

ART² is a 3-D, Monte Carlo RT code based on the original version of Li et al. (2008), which included the continuum emission from X-ray to radio, and an adaptive refinement grid. We have added two more modules, Ly α emission from both recombination and collisional excitation, and ionization of neutral hydrogen, to the current version and couple them self-consistently. The continuum part was described in details in Li et al. (2008). Here we briefly outline the Continuum procedure, and focus on the new implementations of Ly α line and Ionization.

2.1 Continuum Radiative Transfer

The Continuum module in ART² was developed in Li et al. (2008), which adopted the radiative equilibrium algorithm of Bjorkman & Wood (2001). In dusty environments, absorbed radiation energy by dust is re-emitted as thermal emission. The re-emitted spectrum depends on the temperature of the dust, which is assumed to be in thermal equilibrium with the radiation field. The radiative equilibrium is ensured by performing the Monte Carlo transfer iteratively until the dust temperature distribution converges, which can be computationally expensive. To accelerate the calculation, ART² uses the “immediate reemission” scheme (Bjorkman & Wood 2001), in which the dust temperature is immediately updated on absorption of a photon packet, and the frequency of re-emitted photons are sampled from a spectrum that takes into account the modified temperature. The temperature is determined by the balance between the stacked energy absorbed by dust in the cell and the thermal emission from them. The emitted energy in a cell in the time interval Δt is

$$\begin{aligned} E_i^{\text{em}} &= 4\pi\Delta t \int dV_i \int \rho\kappa_\nu B_\nu(T) d\nu \\ &= 4\pi\Delta t\kappa_P(T_i)B(T_i)m_i, \end{aligned} \quad (1)$$

where $\kappa_P = \int \kappa_\nu B_\nu d\nu / B$ is the Planck mean opacity, $B = \sigma T^4 / \pi$ is the frequency integrated Planck function, and m_i is the dust mass in the cell, the subscript i indicates the i 'th cell.

Solving the balance between the absorbed and emitted

energy, we obtain the dust temperature as follows after absorbing N_i packets,

$$\sigma T_i^4 = \frac{N_i L}{4N_\gamma \kappa_P(T_i)m_i}, \quad (2)$$

where N_γ is the total number of photon packets in the simulation, and L is the total source luminosity. Note that because the dust opacity is temperature-independent, the product $\kappa_P(T_i)\sigma T_i^4$ increases monotonically with temperature. Consequently, T_i always increases when the cell absorbs an additional packet.

The added energy to be radiated owing to the temperature increase ΔT is determined by a temperature-corrected emissivity Δj_ν in the following approximation when the temperature increase, ΔT , is small:

$$\Delta j_\nu \approx \kappa_\nu \rho \Delta T \frac{dB_\nu(T)}{dT}. \quad (3)$$

The re-emitted packets, which comprise the diffuse radiation field, then continue to be scattered, absorbed, and re-emitted until they finally escape from the system. This method conserves the total energy exactly, and does not require any iteration as the emergent SED, $\nu L_\nu = \kappa_\nu B_\nu(T)$, corresponds to the equilibrium temperature distribution.

2.2 Ly α Line Transfer

Hydrogen Ly α photon corresponds to the transition between the $n = 2$ and $n = 1$ levels of a hydrogen atom. It is the strongest H I transition. The RT of Ly α photons is determined by Ly α resonant scattering, dust absorption and scattering, and ionization state of the medium. The process is highly complicated in galaxies owing to the complex geometry and gas distribution. In order to accelerate the numerical convergence of the RT process, Monte Carlo method has been commonly used in a number of Ly α codes (e.g., Zheng & Miralda-Escudé 2002; Dijkstra et al. 2006; Tasitsiomi 2006; Verhamme et al. 2006; Laursen et al. 2009a; Pierleoni et al. 2009; Faucher-Giguère et al. 2010). Our implementation of Ly α line transfer adopts the Monte Carlo method, and the major improvements over many of these codes are that, it is coupled with ionization and multi-wavelength continuum which enables a self-consistent and accurate calculation of the Ly α properties, and is incorporated with a 3-D adaptive-mesh refinement grid which efficiently handles arbitrary geometry and inhomogeneous density distribution. Moreover, we treat both recombination and collisional excitation for Ly α emission.

2.2.1 Propagation and Scattering of Ly α Photons

The optical depth $\tau_\nu(s)$ of a Ly α photon with frequency ν traveling a path of length s is determined by

$$\tau_\nu(s) = \int_0^s \int_{-\infty}^{+\infty} n(V_\parallel) \sigma_\nu dV_\parallel dl, \quad (4)$$

where $n(u_\parallel)$ is the number density of neutral hydrogen gas with parallel velocity component V_\parallel , σ_ν is the scattering cross section as a function of frequency. In the rest frame of

the hydrogen atom, σ_ν takes the form

$$\sigma_\nu = f_{12} \frac{\pi e^2}{m_e c} \frac{\Delta\nu_L/2\pi}{(\nu - \nu_0)^2 + (\Delta\nu_L/2)^2} \quad (5)$$

where $f_{12} = 0.4162$ is the Ly α oscillator strength, $\nu_0 = 2.466 \times 10^{15}$ Hz is the line-center frequency, $\Delta\nu_L = 9.936 \times 10^7$ Hz is the natural line width, and the other symbols have their usual meaning. Assuming a Maxwellian distribution for the thermal velocity of the encountering atoms, the resulting average cross section is

$$\sigma_x = f_{12} \frac{\sqrt{\pi} e^2}{m_e c \Delta\nu_D} H(a, x), \quad (6)$$

where

$$H(a, x) = \frac{a}{\pi} \int_{-\infty}^{+\infty} \frac{e^{-y^2}}{(x-y)^2 + a^2} dy \quad (7)$$

is the Voigt function, $\Delta\nu_D = [2k_B T / (m_p c^2)]^{1/2} \nu_0$ is the Doppler width, $x = (\nu - \nu_0) / \Delta\nu_D$ is the relative frequency of the incident photon in the laboratory frame, and $a = \Delta\nu_L / (2\Delta\nu_D)$ is the relative line width.

Some previous work approximated the Voigt function with a Gaussian fitting in the core and a power law fitting in the wing. However, since this approximation causes a relative error of a few tens per cent at the transit region, we use the analytical fit of Tasitsiomi (2006),

$$H(a, x) = q\sqrt{\pi} + e^{-x^2}, \quad (8)$$

where

$$q = \begin{cases} 0 & \text{for } \zeta \leq 0 \\ (1 + \frac{21}{x^2}) \frac{a}{\pi(x^2+1)} \Pi(\zeta) & \text{for } \zeta > 0, \end{cases} \quad (9)$$

with $\zeta = (x^2 - 0.855) / (x^2 + 3.42)$ and $\Pi(\zeta) = 5.674\zeta^4 - 9.207\zeta^3 + 4.421\zeta^2 + 0.1117\zeta$.

This approximation fits the Voigt function well for all frequencies, and the relative error is always less than 1 per cent above a temperature of 2K.

The optical depth of dust absorption and scattering is estimated as,

$$d\tau = n_{\text{HI}} \sigma(\nu) ds + m_d \alpha_d(\nu) ds \quad (10)$$

where m_d is the dust mass and $\alpha_d = \alpha_{d,\text{abs}} + \alpha_{d,\text{sca}}$ is the mass opacity coefficient of absorption and scattering. When the stacked optical depth through passing cells achieves an optical depth determined by Equation (10), the encountering medium is chosen using a random number by comparing with the fraction, $n_{\text{HI}} \sigma(\nu) / (n_{\text{HI}} \sigma(\nu) + m_d \alpha_d(\nu))$.

When Ly α photons are scattered by neutral hydrogen atoms, the frequency in laboratory frame is changed depending on the velocity components of the atoms and the direction of the incidence and the scattering. Then the velocity components of the directions perpendicular to the incident direction will follow a Gaussian distribution, and can be generated by a simple Box-Muller method (Press et al. 1992). However, the parallel component of the velocity depends on relative frequency x of the incident photon owing to the resonance nature of the scattering. The probability distribution of the parallel component is drawn from

$$f(u_{\parallel}) = \frac{a}{\pi H(a, x)} \frac{e^{-u_{\parallel}^2}}{(x - u_{\parallel})^2 + a^2}, \quad (11)$$

where $u_{\parallel} = V_{\parallel} / v_{\text{th}}$ is velocity of the parallel component normalized by thermal velocity v_{th} (hereafter u means normalized velocity by v_{th}). To follow this distribution, we use the method of Zheng & Miralda-Escudé (2002).

When a photon has a frequency $x < x_{\text{cw}}$ in the optically-thick cell, where x_{cw} is the boundary between the core and the wing of the Voigt profile, i.e., where $e^{-x^2} / \sqrt{\pi} = a / \pi x^2$, it cannot travel long distance and is confined in the cell with numerous scattering. Only when it has a large x from scattering by high velocity atoms can it escape from the cell and travel long distance. The photon usually experiences many scatterings ($N \gtrsim 10^3$) before it moves into the wing, it is therefore extremely computation costly to trace this process for all photon packets. In order to speed up the calculation, in particular to avoid the huge number of scatterings in the core, we use a core skipping method developed by Ahn et al. (2002) and follow the procedure of Dijkstra et al. (2006) and Laursen et al. (2009a). It artificially push the photon in the wing by scattering with atoms which have high velocity in the direction perpendicular to the incident direction. The velocity of the perpendicular component u_{\perp} is generated from a truncated Gaussian,

$$\begin{aligned} u_{\perp,1} &= (x_{\text{crit}}^2 - \ln R_1)^{1/2} \cos 2\pi R_2 \\ u_{\perp,2} &= (x_{\text{crit}}^2 - \ln R_1)^{1/2} \sin 2\pi R_2. \end{aligned} \quad (12)$$

where R_1 and R_2 are two univariates, and we use the critical frequency x_{crit} introduced in Laursen et al. (2009a), i.e., $x_{\text{crit}} = 0.02 e^{\xi(\ln a \tau_0)^{\chi}}$ where $(\xi, \chi) = (0.6, 1.2)$ for $a\tau_0 \leq 60$, or $(\xi, \chi) = (1.4, 0.6)$ for $a\tau_0 > 60$. This acceleration scheme can reduce the calculation time by several orders of magnitude, and can produce a line profile which agrees well with analytical solutions in a static slab.

The frequency after scattering depends on the direction in which the photon is scattered. The direction is given by the phase function, $W(\theta) \propto 1 + \frac{R}{Q} \cos^2 \theta$, where θ is the angle between the incident direction n_i and the outgoing direction n_f , and R/Q is the degree of polarization. The ratio R/Q becomes $3/7$ for the $2P_{3/2}$ state in $x < x_{\text{cw}}$ (Hamilton 1940), and 1 for the scattering in the wing (Stenflo 1980). The transition from $2P_{1/2}$ in the core, together with the core skipping scheme, results in isotropic scattering.

The difference in the phase function does not affect the Ly α properties such as the escape fraction f_{esc} , the emergent line profile and luminosity, even if a single phase function is used for all scatterings (e.g., Laursen et al. 2009a). Therefore, we simply assume an isotropic scattering for all the scattering process in this work. We should point out, however, that the phase function becomes important in the polarization effect of Ly α line (e.g., Dijkstra & Loeb 2008), and so care must be taken in dealing with that.

In the scattering process, the final frequency in the laboratory frame is then

$$x_f = x_i - u_{\parallel} + \mathbf{n}_f \cdot \mathbf{u} - g(1 - \mathbf{n}_i \cdot \mathbf{n}_f) \quad (13)$$

where the factor $g = h_P \nu_0 / m_H c v_{\text{th}}$ takes into account the recoil effect (Field 1959; Zheng & Miralda-Escudé 2002) with h_P being the Planck constant. We trace the Ly α photon packet until it is absorbed by dust or escapes from a galaxy (e.g., when the photons move out of the calculation box typically 10 times larger than the virial radius of a galaxy).

2.2.2 Ly α Emissivity

Ly α emission is generated by two major mechanisms: recombination of ionizing photons and collisional excitation of hydrogen gas.

- **Recombination:** Ionizing radiation from stars, AGNs and UVB can ionize the hydrogen gas in galaxies. The collision by high-temperature gas can also ionize the hydrogen. The ionized hydrogen atoms then recombine and create Ly α photons via the state transition $2P \rightarrow 1S$. The Ly α emissivity by the recombination is

$$\epsilon_{\alpha}^{\text{rec}} = f_{\alpha} \alpha_B h\nu_{\alpha} n_e n_{\text{HII}}, \quad (14)$$

where α_B is the case B recombination coefficient, and f_{α} is the average number of Ly α photons produced per case B recombination. Here we use α_B derived in Hui & Gnedin (1997). Since the temperature dependence of f_{α} is not strong, $f_{\alpha} = 0.68$ is assumed everywhere (Osterbrock & Ferland 2006). The product $h\nu_{\alpha}$ is the energy of a Ly α photon, 10.2 eV.

- **Collisional Excitation:** High temperature electrons can excite the quantum state of hydrogen gas by the collision. Due to the large Einstein A coefficient, the hydrogen gas can occur de-excitation with the Ly α emission. The Ly α emissivity by the collisional excitation is estimated by

$$\epsilon_{\alpha}^{\text{coll}} = C_{\text{Ly}\alpha} n_e n_{\text{HI}}, \quad (15)$$

where $C_{\text{Ly}\alpha}$ is the collisional excitation coefficient, $C_{\text{Ly}\alpha} = 3.7 \times 10^{-17} \exp(-h\nu_{\alpha}/kT) T^{-1/2}$ ergs s⁻¹ cm³ (Osterbrock & Ferland 2006).

Once the ionization structure have been determined (see Section 2.3), we estimate the intrinsic Ly α emissivity in each cell by the sum of above Ly α emissivity, $\epsilon_{\alpha} = \epsilon_{\alpha}^{\text{rec}} + \epsilon_{\alpha}^{\text{coll}}$. The excitation cooling dominates at $T_{\text{gas}} \sim 10^{4-5}$ K, but becomes smaller than the recombination cooling at $T_{\text{gas}} \gtrsim 10^6$ K (e.g., Faucher-Giguère et al. 2010).

There is a large ambiguity in the estimation of the excitation cooling from multi-component ISM in SPH simulations (Faucher-Giguère et al. 2010). However, in the present work, we find that the power from stars and AGNs is always larger than or comparable with the excitation cooling. Hence, even the largest possible cooling rate is still subdominant to the nebular Ly α emission (i.e., coming from HII regions around young hot stars). In this paper, we estimate the ionization rate and Ly α emissivity for each cell by using the mixed physical quantities of multi-component ISM at first, then reduce it by weighting with the mass fraction of cold gas f_{cold} , i.e., $\epsilon_{\alpha}^{\text{coll}} = \epsilon_{\alpha,0}^{\text{coll}} \times (1 - f_{\text{cold}})$, where f_{cold} can reach ~ 0.9 depending on the situation.

2.2.3 Test Calculations

To test our implementation of the Ly α RT, we perform some standard tests against analytical solutions, as well as other numerical results in the literature.

1. Neufeld Test

As the first test, we carry out the RT calculation in a dust-free slab of uniform gas. The uniform slab was analytically studied by Neufeld (1990) in the optically thick limit.

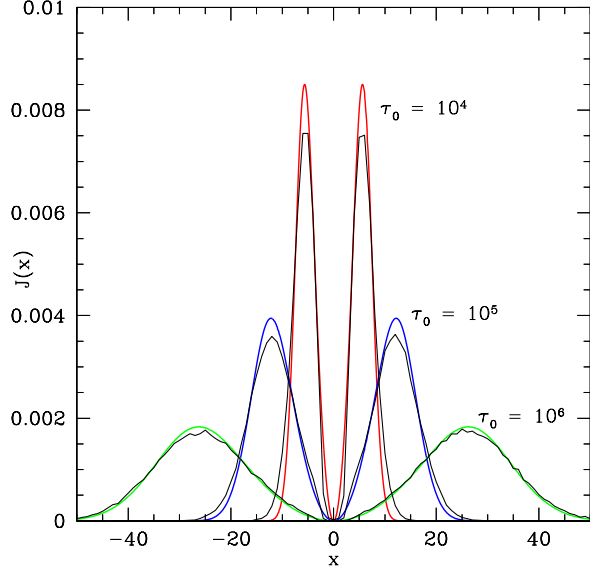


Figure 1. The Neufeld Test of emergent Ly α profiles of monochromatic line radiation emitted from a dust-free uniform slab. The black lines are our simulation results, and the color lines represent analytical solutions by Neufeld (1990) for different optical depths: red – $\tau_0 = 10^4$, blue – $\tau_0 = 10^5$, and green – $\tau_0 = 10^7$. The temperature of gas is 10 K.

In this case, the emergent Ly α line profile is given by

$$J(\pm\tau_0, x) = \frac{\sqrt{6}}{24} \frac{x^2}{\sqrt{\pi} a \tau_0} \frac{1}{\cosh[\sqrt{\pi^3/54}(x^3 - x_{\text{inj}}^3)/a\tau_0]}, \quad (16)$$

where τ_0 is the optical depth at the line center from mid-plane to the boundary of the slab and x_{inj} is the injection frequency x .

Figure 1 shows our test result of emergent spectra from a dust-free gas slab with a temperature of $T = 10$ K and a central plane source, in comparison with analytical solutions for optical depths $\tau_0 = 10^4, 10^5$ and 10^6 , respectively. The width of the peaks becomes larger with larger τ_0 , in agreement with the dependence of the optical depth on frequency. Our simulation results agree very well with the analytical solutions, and the agreement becomes better with higher τ_0 .

The dust absorption is crucial in the study of escape fraction, flux, image and profile of Ly α from galaxies. Neufeld (1990) has derived an approximate expression for the escape fraction of Ly α photons in a static dusty slab,

$$f_{\text{esc}} = \frac{1}{\cosh\left[\zeta' \sqrt{(a\tau_0)^{1/3} \tau_a}\right]}, \quad (17)$$

where τ_a is the absorption optical depth of dust, and $\zeta' \equiv \sqrt{3}/\zeta \pi^{5/12}$, with $\zeta \simeq 0.525$ being a fitting parameter. This solution is valid for extremely optically thick which $a\tau_0 \geq 10^3$, and in the limit of $(a\tau_0)^{1/3} \gg \tau_a$. It suggests that the escape fraction decreases rapidly with increasing $(a\tau_0)^{1/3} \tau_a$.

In figure 2, we compare our simulation results of Ly α escape fraction in a dusty slab with the analytical solutions of Neufeld (1990). As is shown, our results agree with the analytical curve very well.

2. Loeb & Rybicki Test

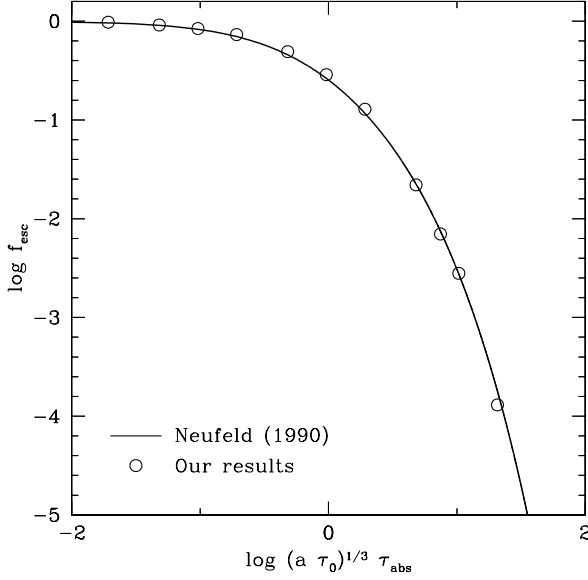


Figure 2. The Neufeld Test of escape fraction of Ly α photons in a dusty slab as a function of $(a \tau_0)^{1/3} \tau_{\text{abs}}$. The solid line is an approximate analytical solution of Neufeld (1990), and the open circles are our simulation results.

Loeb & Rybicki (1999) analytically derived the intensity field in a spherically symmetric, uniform, radially expanding neutral hydrogen cloud surrounding a central point source of Ly α photons. No thermal motion is included ($T = 0$ K). In the diffusion limit, the mean intensity $\tilde{J}(\tilde{r}, \tilde{\nu})$ as a function of distance from the source \tilde{r} and frequency shift $\tilde{\nu}$ is given by

$$\tilde{J} = \frac{1}{4\pi} \left(\frac{9}{4\pi\tilde{\nu}^3} \right)^{3/2} \exp\left(-\frac{9\tilde{r}^2}{4\tilde{\nu}^3}\right), \quad (18)$$

with $\tilde{\nu} = (\nu_0 - \nu)/\nu_*$, where ν_* is the comoving frequency shift of Ly α at which the optical depth to infinity is unity, and $\tilde{r} = r/r_*$ is the scaled distance, where r_* is the physical distance at which the Doppler shift from the source due to the Hubble-like expansion equals ν_* .

We use a simulation setup similar to that of Semelin, Combes, & Baek (2007) for the test. The results are presented in Figure 3 in comparison with the analytical solutions of Loeb & Rybicki (1999). Our simulation results are very close to those from previous tests (e.g., Tasitsiomi 2006; Semelin et al. 2007), and are in good agreement with the analytical solutions in regimes where the diffusion limit is valid. However, the simulations diverge from the analytic solutions at larger \tilde{r} , where the assumption of optically thick is no longer valid.

3. Bulk Motion Test

The bulk motion of gas affects the escape of Ly α photons as it decreases the effective optical depth (Dijkstra et al. 2006; Laursen et al. 2009a). In practice, the bulk speed of the gas to the center can be $\sim 10\text{--}1000 \text{ km s}^{-1}$ for inflow caused by gravitation, or outflow by supernovae. The relative velocity can decrease the optical depth significantly. Unfortunately, there is no analytical solution of

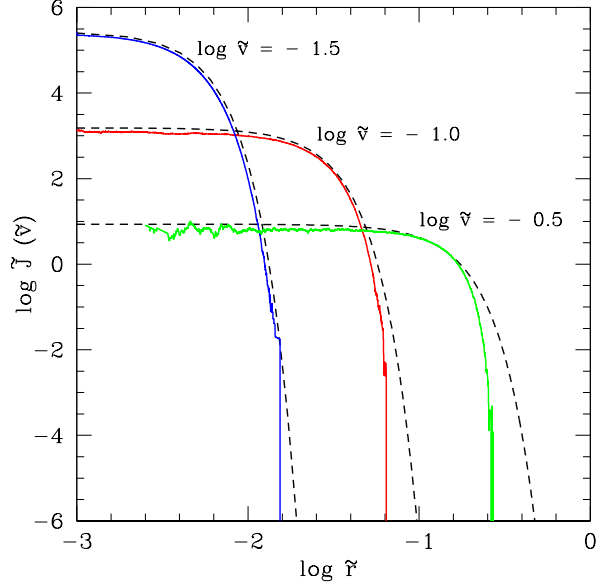


Figure 3. The Loeb & Rybicki Test of mean intensity profiles of a monochromatic Ly α source in a uniformly expanding medium at various frequencies. The dotted lines are analytical solutions by Loeb & Rybicki (1999) in the diffusion limit, and the color lines are our simulation results.

emergent spectrum for moving medium of $T \neq 0$ K. However, Laursen et al. (2009a) calculated the emergent spectra of an isothermal and homogeneous sphere undergoing isotropic expansion or contraction. Here, we follow the procedure of Laursen et al. (2009a) to set up the test. The velocity $\mathbf{v}_{\text{bulk}}(\mathbf{r})$ of a fluid element at a distance \mathbf{r} from the center is set to be

$$\mathbf{v}_{\text{bulk}}(\mathbf{r}) = \mathcal{H}\mathbf{r}, \quad (19)$$

where the Hubble-like parameter \mathcal{H} is fixed such that the velocity increases linearly from 0 in the center to a maximal absolute velocity v_{max} at the edge of the sphere ($r = R$):

$$\mathcal{H} = \frac{v_{\text{max}}}{R}, \quad (20)$$

with v_{max} positive for an expanding sphere, or negative for a collapsing one.

Figure 4 shows the our test results of the emergent spectrum from an isothermal and homogeneous sphere undergoing isotropic expansion with different maximal velocities v_{max} at the edge of the sphere. As v_{max} increases, the blue wing is suppressed while the red wing is broadened. This is because in an outflowing sphere, the photons in the blue wing have a higher probability of encountering hydrogen atoms and being scattered than those in the red wing, which can escape more easily. This plot suggests that the peak of the profile is pushed further away from the line center for increasing v_{max} . However, above a certain threshold value, the peak moves back toward the center again owing to the decrease of optical depth caused by the fast bulk motion. Our results show a good agreement with the previous simulations by Laursen et al. (2009a).

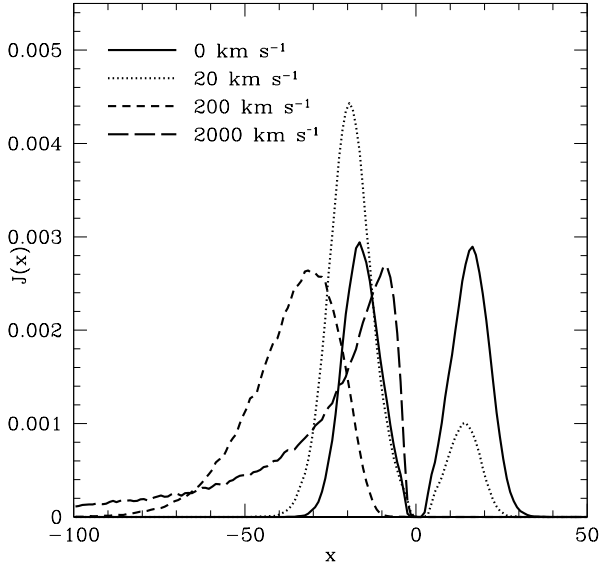


Figure 4. Bulk Motion Test of emergent Ly α spectrum from an isothermal and homogeneous sphere undergoing isotropic expansion with different maximal velocities at the edge of the sphere. The initial conditions are the same as those used for Figure 8 in Laursen et al. (2009a), with a temperature of the sphere $T = 10^4$ K, and the hydrogen column density $N_{\text{HI}} = 2 \times 10^{22} \text{ cm}^{-2}$.

2.3 Ionization Radiative Transfer

Ionizing photons from young stars play an important role in galaxy evolution and the cosmic reionization of the intergalactic medium (IGM) in the early universe. Stellar radiation can ionize interstellar gas, and a fraction of them can escape from galaxies, and reionize the neutral hydrogen (e.g., Iliiev et al. 2007; Gnedin, Kravtsov, & Chen 2008; Razoumov & Sommer-Larsen 2010; Yajima et al. 2009; Yajima, Choi, & Nagamine 2011). The ionization structure in IGM is highly relevant to the detectability of high- z LAEs (e.g., McQuinn et al. 2007; Dayal et al. 2011). In particular, ionization affects significantly the properties of distant LAEs, as the emissivity, scattering and escaping of Ly α photons depend sensitively on the ionization state of the ISM.

The existing algorithms of ionization RT can be broadly divided into three categories: moments, Monte Carlo, and ray-tracing methods (see Trac & Gnedin 2011 for a recent review). Recently, Iliiev et al. (2006) and Iliiev et al. (2009) conducted a comparison of various cosmological ionization codes. It was shown that the ray-tracing method provides the most accurate solution but is computationally expensive (e.g., Gnedin & Ostriker 1997; Umemura, Nakamoto, & Susa 1999; Abel, Norman, & Madau 1999; Abel & Wandelt 2002; Razoumov et al. 2002; Mellema et al. 2006; Susa 2006; Hasegawa & Umemura 2010), the moments method is usually diffusive (e.g., Gnedin & Abel 2001), and the Monte Carlo method is efficient and flexible but requires a large number of photon packets (e.g., Ciardi et al. 2001; Maselli, Ferrara, & Ciardi 2003; Pierleoni et al. 2009).

Our implementation of the ionization RT in ART² code

is based on the Monte Carlo method, which is similar to CRASH (Maselli et al. 2003).

2.3.1 Basic Equations and Methods

The RT of ionizing photons in our code also includes absorption and scattering process by hydrogen gas and interstellar dust. The optical depth is estimated similar to equation (10), $d\tau = n_{\text{HI}}\sigma_{\text{H}^0}(\nu)ds + m_{\text{d}}\alpha_{\text{d}}(\nu)ds$, where $\sigma_{\text{H}^0}(\nu) = 6.3 \times 10^{-18}(\nu/\nu_{\text{L}})^{-3}$ is the ionizing cross section of hydrogen with Lyman limit frequency ν_{L} (Osterbrock 1989). The time evolution of ionization degree of hydrogen gas is estimated by

$$n_{\text{H}} \frac{dX}{dt} = k_{\text{star}}^{\gamma} n_{\text{HI}} + k_{\text{UVB}}^{\gamma} n_{\text{HI}} + k^{\text{C}} n_{\text{HI}} n_{\text{e}} - \alpha_{\text{rec}} n_{\text{HI}} n_{\text{e}}, \quad (21)$$

where k_{star}^{γ} , k_{UVB}^{γ} are the photo-ionization efficiency by star and UVB, respectively, k^{C} is the collisional-ionization efficiency, and α_{rec} is the recombination coefficient. Both k^{C} and α_{rec} are taken from Cen (1992). The k^{γ} by UVB is estimated by self-shielding model, in which UVB is optically thin at $n_{\text{H}} < n_{\text{crit}}$, zero intensity at $n_{\text{H}} \geq n_{\text{crit}}$. We set the critical density to be $n_{\text{crit}} = 0.0063 \text{ cm}^{-3}$ based on the observation data of column density distribution of neutral hydrogen gas (Nagamine, Choi, & Yajima 2010).

The photo-ionization rate by stars and AGNs is estimated by absorbed-photon number in a cell $N_{\text{abs}}^{\text{ion}}$, i.e., $k_{\text{star}}^{\gamma} n_{\text{HI}} = N_{\text{abs}}^{\text{ion}}$. We treat the time integration with an adaptive time step introduced in Baek et al. (2009), by using three time steps, Δt_{evo} , Δt_{RT} and Δt_{rec} , where Δt_{evo} is an evolution time step to renew the ionization state. It is determined by splitting the recombination time scale of volume-mean density by ~ 100 , which is close to that of low-density region. In each Δt_{evo} , the photon-budget of N_{ph} are traced and the ionization rate is estimated. The evolution of ionization degree is renewed with Δt_{evo} , which is divided by Δt_{rec} , a time step estimated from recombination time-scale in each cell such that the ionization rate is constant. However, when the ratio of the absorbed photon number to that of neutral hydrogen in a cell exceeds a pre-set limit ($= 0.25$ in this work), the ionization fraction is renewed with Δt_{RT} .

In addition, the frequency of the photon is sampled from the source spectrum, similar to that in the continuum RT calculation. We use the stellar population synthesis model of GALAXEV (Bruzual & Charlot 2003) to produce intrinsic SEDs of stars for a grid of metallicity and age, and we use a simple, broken power law for the AGN (Li et al. 2008). A Salpeter (1955) initial mass function is used in our calculations.

2.3.2 Test Calculations

To test our code, we simulate an HII bubble by a central point source in a hydrogen sphere with uniform density, i.e., the Strömgren sphere (Strömgren 1939). The radius of the HII bubble, r_{s} , is estimated by the balance between the ionization rate of the source and the recombination rate of the gas

$$r_{\text{s}} = \left(\frac{3N_{\text{ion}}}{4\pi\alpha_{\text{B}}n_{\text{H}}^2} \right)^{\frac{1}{3}}, \quad (22)$$

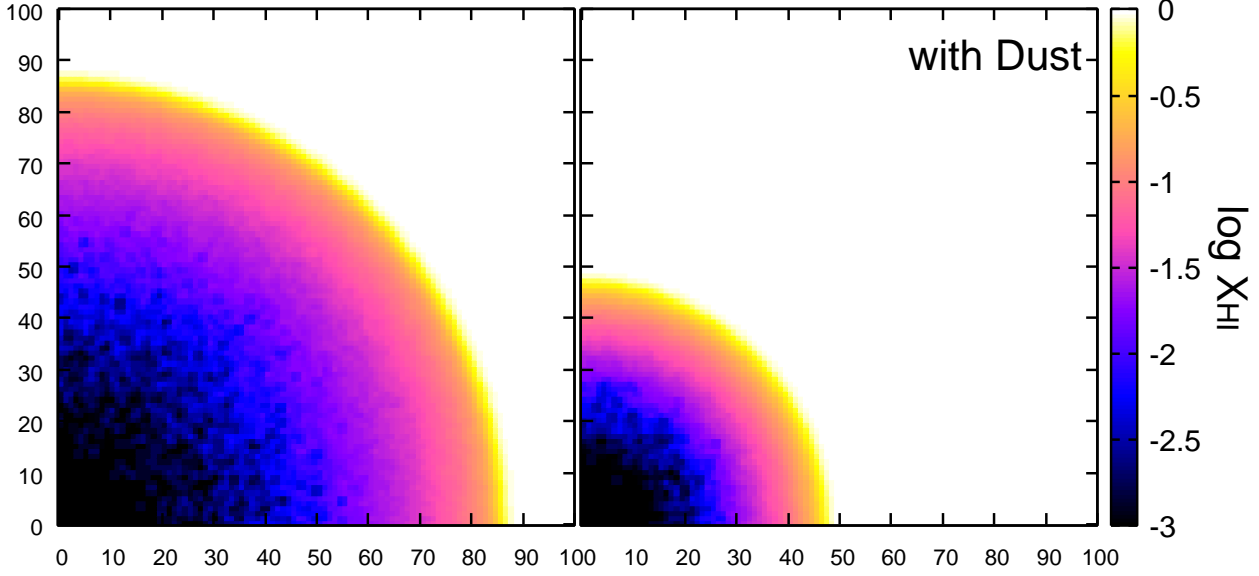


Figure 5. Ionization structure by a point source in a uniform density field. The color bar indicates the neutral fraction of the hydrogen gas in log scale. Left panel: dust-free medium with $n_{\text{H}} = 10^{-3} \text{ cm}^{-3}$, and right panel: dusty medium with $n_{\text{H}} = 10^{-3} \text{ cm}^{-3}$ and $\tau_{\text{Sd}} = 4.0$, where τ_{Sd} is a optical depth of dust absorption from source to the radius of the Strömgren sphere. The source is placed at corner of the simulation box with $\dot{N}_{\text{ion}} = 5 \times 10^{48} \text{ s}^{-1}$, and the cell size is 66.7 pc.

where N_{ion} is the number of ionizing photons from the source per second, and α_{B} is the recombination coefficient to all excitation states.

And the position of the ionizing front of the HII bubble, r_{i} is analytically derived by Spitzer (1978),

$$r_{\text{i}} = r_{\text{s}} \left(1 - e^{-\frac{t}{t_{\text{rec}}}} \right)^{\frac{1}{3}}, \quad (23)$$

where t_{rec} is the recombination timescale. When $t \gg t_{\text{rec}}$, r_{i} approaches to r_{s} .

In the presence of dust, the size of HII bubble decreases due to dust extinction. Spitzer (1978) has also derived analytically the size of the HII bubble r_{i} in a dusty medium:

$$3 \int_0^{y_{\text{i}}} y^2 e^{y\tau_{\text{Sd}}} dy = 1, \quad (24)$$

where $y = r/r_{\text{s}}$, $y_{\text{i}} = r_{\text{i}}/r_{\text{s}}$, and τ_{Sd} is the optical depth of dust from the source to the distance of Strömgren sphere.

In the tests, we calculate the ionization structure of a uniform density field. The source is placed at the corner of the simulation box with $N_{\text{ion}} = 5 \times 10^{48} \text{ s}^{-1}$. The number density is $n_{\text{H}} = 10^{-3} \text{ cm}^{-3}$, and the recombination coefficient $\alpha_{\text{B}} = 2.59 \times 10^{-13} \text{ cm}^3 \text{ s}^{-1}$ ($T = 10^4 \text{ K}$).

Figure 5 shows the neutral fraction of hydrogen gas at mid-plane at $t = 3t_{\text{rec}}$, in a dust-free (left panel) and a dusty medium (right panel). The HII bubble becomes significantly smaller than that in dust-free medium. Figure 6 shows the corresponding neutral fraction of hydrogen gas as a function of the distance from the source for both dust-free and dusty tests, and Figure 7 shows the position of the ionization front of the dust-free medium. All our results are in good agreements with the analytical solutions of Spitzer (1978).

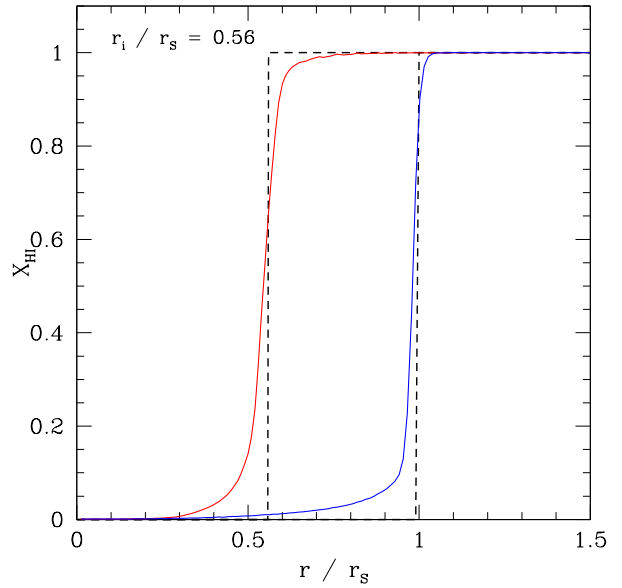


Figure 6. Neutral fraction of hydrogen gas in log scale as a function of distance from source in a dust-free uniform medium. The distance is normalized by the radius of Strömgren sphere. The color lines represent our simulation results for a dust-free (blue line) and a dusty medium with $\tau_{\text{Sd}} = 4.0$ (red line), and the dotted lines are the analytical solutions by Spitzer (1978).

2.4 Adaptive Refinement Grid

Our RT calculation is done on a grid. In order to handle arbitrary geometry, and cover a large dynamical range while resolving small-scale, high-density gas regions in galaxies and

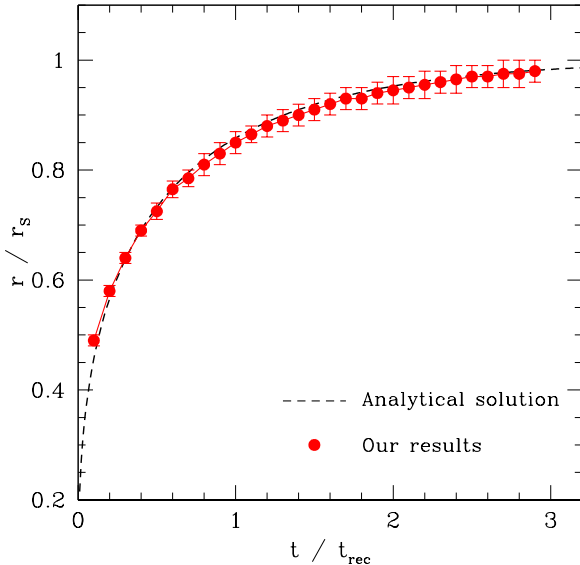


Figure 7. Time evolution of the HII region radius in a dust-free uniform medium. The dotted line is the analytical solution by Spitzer (1978), and the red filled circles are our simulation results. The error bars indicate the radius of neutral fraction of 0.3 – 0.7.

ISM, we use an adaptive-mesh refinement grid in 3-D Cartesian coordinates. The detailed description of the adaptive grid is given in Li et al. (2008). Here we briefly summarize the basic method and procedures.

We typically start with a base grid of 4^3 box covering the entire simulation volume. Each cell is then adaptively refined by dividing it into 2^3 sub-cells. The refinement is stopped if a predefined maximum refinement level, RL, is reached, or if the total number of particles in the cell becomes less than a certain threshold (typically set to be 32 for SPH simulations), whichever criterion is satisfied first. The resolution of the finest level is therefore $L_{\min} = L_{\text{box}}/2^{\text{RL}+1}$, where L_{box} is the box length, and RL is again the maximum refinement level.

The ART² code can be easily applied to either grid- or particle-based simulations, once the snapshot is converted to the format of our grid, which is an effective octo-tree. For particle-based simulations, the physical quantities of particles are interpolated onto a grid. For example, the gas properties at the center of each grid cell, such as density, temperature, and metallicity, are calculated using the SPH smoothing kernel of the original simulation. All physical quantities are assumed to be uniform across a single cell.

Figure 8 shows an example of the adaptive grid applied to a snapshot redshift $z = 3.1$ from the cosmological simulation used in this work (see Section 3.1 for details). For the parameters used in this application, $L_{\text{box}} = 1$ Mpc, RL = 11, we use a total grid number of only ~ 58300 and reach a minimum cell size of $L_{\min} = 59.5$ pc in physical scale, which corresponds to the spatial resolution of 244 pc in comoving scale of the hydrodynamic simulation. This grid resolution is equivalent to a $\sim 4096^3$ uniform grid, which is prohibitive with current computational capabilities.

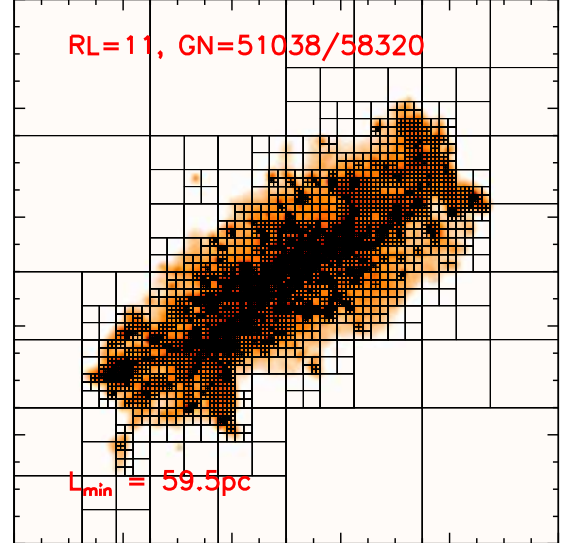


Figure 8. Example of the adaptive grid applied to a snapshot at redshift $z = 3.1$ from the cosmological simulation on top of the gas density distribution of the system. The box size is 1 Mpc in comoving scale. The maximum refinement level is 11, and the size of the finest cell is 59.5 pc in physical scale.

2.5 ISM Model

ART² implements a multi-phase model of the ISM (McKee & Ostriker 1977), as adopted in the hydrodynamic simulations (Springel & Hernquist 2003a,b). It consists of a “hot-phase” (diffuse) and a “cold-phase” (dense molecular and HI core) components, which co-exist under pressure equilibrium but have different mass fractions and volume filling factors (i.e., the hot-phase gas is ≤ 0.1 in mass but $\gtrsim 0.99$ in volume). The cold gas is assumed to follow two empirical relations observed in giant molecular clouds: a power-law mass distribution (e.g., Larson 1981; Fuller & Myers 1992; Ward-Thompson et al. 1994; Andre, Ward-Thompson, & Motte 1996; Blitz & Rosolowsky 2006), and a power-law mass-radius relation (e.g., Sanders, Scoville, & Solomon 1985; Dame et al. 1986; Scoville et al. 1987; Solomon et al. 1987; Rosolowsky 2005, 2007). Within each grid cell in the RT calculation, the hot gas is uniformly distributed, while the cold, dense cores are randomly embedded.

The dust is assumed to be associated with both the cold and hot phase gases, and it follow the distribution of the gas with certain dust-to-gas ratio. In the RT calculation, when a photon enters a cell, we first determine the distance it travels in the hot phase gas before hitting a cold cloud, then the distance it travels in the cold cloud before it is absorbed. The combination of the two gives the total optical depth in the multi-phase ISM, which is then compared with a random number to determine whether the photon should be stopped for scattering or absorption (see Li et al. 2008

for a detailed description and implementation). The Ly α RT in a multi-phase ISM and dust model is one of the new features in our RT code compared with previous works. In ART², depending on the hydrodynamic simulation and the nature of the calculation, we can choose either a multi-phase or a single-phase model, in which the gas and the dust are uniformly distributed with the mean density in a cell, for the ISM.

Galaxies and quasars at high redshifts show extinction by interstellar dust (Ouchi et al. 2004; Maiolino et al. 2004). In the early universe, most of the dust is thought to be created by Type II supernovae (SNe). Theoretically, several groups have calculated dust formation in the ejecta of Type II SNe (Todini & Ferrara 2001; Nozawa et al. 2003; Schneider, Ferrara, & Salvaterra 2004; Hirashita et al. 2005; Dwek, Galliano, & Jones 2007). In particular, Todini & Ferrara (2001) have developed a dust model based on standard nucleation theory and tested it on the well-studied case of SN1987A. They find that SNe with masses in the range of 12 – 35 M_{\odot} produce about 0.01 of the mass in dust per supernova for primordial metallicity, and ~ 0.03 for solar metallicity.

In ART², we adopt the dust size distribution of Todini & Ferrara (2001) for solar metallicity and a $M = 22 M_{\odot}$ SN model, as in Figure 5 in their paper. The size distribution is then combined with the dust absorption and scattering cross section of Weingartner & Draine (2001) to calculate dust absorption opacity curves. The SN models include silicate fractions $f_s = 0.1$, which shows the silicate feature $\sim 9.7 \mu\text{m}$ (see the resultant opacity curve Li et al. (2008)). The dust-to-gas mass ratio in each cell is linearly proportional to the metallicity in the cell. The ratio is normalized to Galactic value when the metallicity is the solar abundance.

2.6 Coupling Ionization, Ly α Line, and Continuum

To date, there is little work on the coupling of continuum and Ly α line transfer. In the seminar work of Pierleoni et al. (2009), they incorporated pre-computed tables of the properties of the Ly α photons in the calculation of ionizing UV continuum radiation. Our approach differs from theirs in that we follow the actual propagation and scattering of the Ly α photons in the medium, and take into account the effects of ionization and dust absorption.

In ART², the photons are treated in three regimes: ionizing continuum at $\lambda \leq 912 \text{ \AA}$, Ly α line with center $\lambda = 1216 \text{ \AA}$, and non-ionizing continuum at $912 \text{ \AA} < \lambda \leq 10^7 \text{ \AA}$. We follow the following steps to couple the radiative transfer of these three components:

1. The gas and dust content of each grid cell is determined before the RT process.
2. The neutral hydrogen fraction n_{HI} in each cell is determined by following the ionizing continuum photons.
3. The resulting ionization structure is then input to calculate the RT of Ly α photons.
4. The absorption of the ionizing photons by dust will be taken into account in the calculation of the dust re-emission in longer wavelengths of the non-ionizing continuum.

2.7 Monte Carlo Method

The Monte Carlo RT method follows the propagation, scattering, absorption, and reemission of “photon packets” (groups of equal-energy, monochromatic photons that travel in the same direction), by randomly sampling the various probability distribution functions that determine the optical depth, scattering angle, and absorption rates. In detail, the Monte Carlo ray-tracing procedure involves the following steps:

1. A photon packet of continuum is emitted from either a stellar source or an accreting black hole with random frequencies consistent with the source spectra. In the case of Ly α photon, it is emitted from ionized hydrogen gas. The photon is emitted with a uniformly distributed random direction. The probability of a photon being emitted by any given source is determined by its luminosity relative to the total.

2. A random optical depth over which the photon must travel before an interaction with gas or dust occurs, $\tau_i = -\ln\xi$, is drawn to determine the interaction location. The interaction includes scattering and absorption. In our method, the photon energies are not weighted, only one event is allowed. That is, at any given interaction site, the photon is either scattered or absorbed, but not both.

3. Starting from the location of the photon emission, the cumulative optical depth of the photon, τ_{tot} , is calculated stochastically for both hot and cold ISM in a multi-phase model, or single-phase medium with the mean density along the ray. If the photon is stopped for interaction within a single cell, then τ_{tot} is the sum of contributions from possibly multiple segments of both hot and cold for the multi-phase model, or a single-phase gas/dust within this cell. If the photon passes through multiple cells before an interaction occurs, then τ_{tot} is the sum of all contributions from relevant segments in these cells.

4. At each boundary between the hot and cold phase gas clouds, or at the boundary of the grid cell, the next interaction point is determined by the comparison between τ_i and τ_{tot} . If $\tau_i \leq \tau_{\text{tot}}$, then the photon is either scattered or absorbed, with a probability given by the scattering albedo. The exact interaction location is then determined inside either hot or cold phase gas, such that τ_{tot} becomes exactly τ_i . If the photon is scattered, its direction is altered using a phase function, and the ray tracing of the new photon is repeated from step 2. The phase function is the Henyey-Greenstein for dust, and simply isotropic for gas. If the photon is absorbed by dust, the dust temperature is raised, and a new photon is re-emitted according to the scheme described below. The ray tracing of the newly emitted photon again restarts from step 2.

5. If the photon escapes from the system without reaching the optical depth τ_i , it is then collected in the output spectrum and image. The next photon will be picked up from the source, and the whole Monte Carlo procedure from step 1 will be restarted.

2.8 Making Images

In ART², we incorporate a “peeling off” procedure using weighted photons to obtain high-resolution images from a

particular viewing direction. From a particular viewing direction, the contribution from direct (radiation source or thermal dust emission) and scattered photons are tracked separately with different weight.

At each location of emission, the contribution from direct photons to the image is computed as

$$I_{\text{direc}}(x, y) = I_0 \frac{e^{-\tau_1}}{4\pi d^2}, \quad (25)$$

where I_0 is the energy of each photon packet, x and y are the position of the emission site projected onto the image plane, and τ_1 and d are the total optical depth and distance from the emission site to the observer, respectively.

At each scattering site, the contribution from scattered photons to the image is

$$I_{\text{scatt}}(x, y) = I_0 \frac{e^{-\tau_2} f(\theta)}{d^2}, \quad (26)$$

where τ_2 is the optical depth from the scattering location to the observer, and $f(\theta)$ is the scattering phase function.

The total intensity of the image is the sum of I_{direct} and I_{scatt} , and is accumulated as each photon packet is emitted and scattered during the course of the Monte Carlo simulation. To obtain an image for a given telescope at a given waveband, a specific filter function is then applied to convolve the image.

3 APPLICATION TO COSMOLOGICAL SIMULATIONS

3.1 The Simulations

The cosmological simulation presented here follows the formation and evolution of a Milky Way-size galaxy and its substructures. The simulation includes dark matter, gas dynamics, star formation, black hole growth, and feedback processes. The initial condition is originally from the Aquarius Project (Springel et al. 2008), which produced the largest ever particle simulation of a Milky Way-sized dark matter halo. The hydrodynamical initial condition is reconstructed from the original collisionless one by splitting each original particle into a dark matter and gas particle pair, displaced slightly with respect to each other (at fixed center of mass) for a regular distribution of the mean particle separation, and with a mass ratio corresponding to a baryon fraction of 0.16 (Wadepuhl & Springel 2011).

The whole simulation falls in a periodic box of $100 h^{-1} \text{Mpc}$ on each side with a zoom-in region of a size $5 \times 5 \times 5 h^{-3} \text{Mpc}^3$. The spatial resolution is $\sim 250 h^{-1} \text{pc}$ in the zoom-in region. The mass resolution of this zoom-in region is $\sim 2 \times 10^5 h^{-1} M_\odot$ for dark matter particles, $\sim 1.9 \times 10^4 h^{-1} M_\odot$ for gas and star particles. The cosmological parameters used in the simulation are $\Omega_m = 0.25$, $\Omega_\Lambda = 0.75$, $\sigma_8 = 0.9$ and $h = 0.73$, consistent with the five-year results of the WMAP (Komatsu et al. 2009). The simulation evolves from $z = 127$ to $z = 0$.

The simulation was performed using the parallel, N-body/Smoothed Particle Hydrodynamics (SPH) code GADGET-3, which is an improved version of that described in Springel, Yoshida, & White (2001) and Springel (2005). For the computation of gravitational forces, the

code uses the “TreePM” method (Xu 1995) that combines a “tree” algorithm (Barnes & Hut 1986) for short-range forces and a Fourier transform particle-mesh method (Hockney & Eastwood 1981) for long-range forces. GADGET implements the entropy-conserving formulation of SPH (Springel & Hernquist 2002) with adaptive particle smoothing, as in Hernquist & Katz (1989). Radiative cooling and heating processes are calculated assuming collisional ionization equilibrium (Katz et al. 1996; Davé et al. 1999). Star formation is modeled in a multi-phase ISM, with a rate that follows the Schmidt-Kennicutt Law (Schmidt 1959; Kennicutt 1998). Feedback from supernovae is captured through a multi-phase model of the ISM by an effective equation of state for star-forming gas (Springel & Hernquist 2003a). The UV background model of Haardt & Madau (1996) is used.

Black hole growth and feedback are also included in our simulation based on the model of Springel, Di Matteo, & Hernquist (2005b); Di Matteo, Springel, & Hernquist (2005), where black holes are represented by collisionless “sink” particles that interact gravitationally with other components and accrete gas from their surroundings. The accretion rate is estimated from the local gas density and sound speed using a spherical Bondi-Hoyle (Bondi 1952; Bondi & Hoyle 1944; Hoyle & Lyttleton 1941) model that is limited by the Eddington rate. Feedback from black hole accretion is modeled as thermal energy, $\sim 5\%$ of the radiation, injected into surrounding gas isotropically, as described in Springel et al. (2005b) and Di Matteo et al. (2005). This feedback scheme self-regulates the growth of the black hole and has been demonstrated to successfully reproduce many observed properties of local elliptical galaxies (e.g., Springel, Di Matteo, & Hernquist 2005a; Hopkins et al. 2006) and the most distant quasars at $z \sim 6$ (Li et al. 2007). We follow the black hole seeding scheme of Li et al. (2007) and Di Matteo et al. (2008) in the simulation: a seed black hole of mass $M_{\text{BH}} = 10^5 h^{-1} M_\odot$ was planted in the gravitational potential minimum of each new halo identified by the friends-of-friends (FOF) group finding algorithms with a total mass greater than $10^{10} h^{-1} M_\odot$.

Each snapshot is processed by an on-flying FOF group finding algorithm with a dark matter linking length less than 20% of their mean spacing. Other types of particles are then linked to the nearest dark matter particle. A substructure detection algorithm SUBFIND (Dolag et al. 2009) is then applied to each group to search satellite halos. In the simulation, each FOF group with its substructure is identified as a galaxy (a detailed description of the simulation is presented in Zhu et al., in preparation).

In this work, we apply the ART² code to the ten most massive galaxies in each snapshot at six redshift bins from $z = 3.1 - 10.2$ and focus on the Ly α and multi-band properties. In our post-processing procedure, we first calculate the RT of ionizing photons ($\lambda \leq 912 \text{ \AA}$) and estimate the ionization fraction of the ISM. The resulting ionization structure is then used to run the Ly α RT to derive the emissivity, followed by the calculation of non-ionizing continuum photons ($\lambda > 912 \text{ \AA}$) in each cell. Our fiducial run is done with $N_{\text{ph}} = 10^5$ photon packets for each ionizing, Ly α , and non-ionizing components. Because the spatial resolution of the cosmological simulation is not adequate to resolve the mul-

multiple phase of the ISM, we assume a single-phase medium in each density grid. The highest refinement of the grid is $RL = 11$.

3.2 Multi-wavelength Properties of High-redshift Galaxies

3.2.1 Flux Images

The galaxies in our sample are the 10 most massive ones from the cosmological simulation at six snapshots from $z = 3.1 - 10.2$. Note that because our simulation focuses on a Milky Way-size galaxy, our sample represents the progenitors of the Milky Way at different cosmic time, they are not the typical “massive” galaxies one expect from a general cosmological simulation with a mean overdensity. The total and stellar masses of these galaxies become larger with time (decreasing redshift) due to gas accretion and merging process. For example, the total mass of the most massive galaxy is $\sim 2.6 \times 10^{10} M_\odot$, $5.8 \times 10^{10} M_\odot$, $1.6 \times 10^{11} M_\odot$, and $5.4 \times 10^{11} M_\odot$ at $z = 10.2, 8.5, 6.2$ and 3.1 respectively, and the corresponding stellar mass is $\sim 8.5 \times 10^8 M_\odot$, $4.3 \times 10^9 M_\odot$, $9.3 \times 10^9 M_\odot$, and $4.1 \times 10^{10} M_\odot$.

Figure 9 (left panels) show the projected density of gas and stars of each snapshot at the mentioned redshift. Filamentary structure is clearly seen, and the most massive galaxy resides in the intersection of the filaments. The resulting Ly α and near infrared (NIR) fluxes of the most massive galaxy from our RT calculations are shown in the middle and right panels of Figure 9, respectively. The NIR band corresponds to IRAC-1 ($3.6 \mu\text{m}$) of the *Spitzer* telescope. The flux image is generated from a “peeling off” technique in the RT calculation as described in Section 2.8.

The Ly α emission appears to follow the distribution of gas and stars of the galaxy. Its surface brightness and size increase with time (decreasing redshift), while those of the NIR show different pattern. The Ly α emission depend on the star formation rate (SFR) of the galaxy and the photon escape fraction. Although SFR decreases at lower redshift, the escape fraction increases as the galaxy grows larger, resulting in an increase of Ly α luminosity. In addition, the Ly α emission is bright over extended region, owing to many scattering processes.

On the other hand, the observed IRAC-1 in these redshifts corresponds to wavelengths $\sim 3200 - 9000 \text{ \AA}$ in the rest frame, hence it depends on both SFR and stellar mass of the galaxy. The cross section of dust decreases steeply with increasing wavelength, it becomes very small at these wavelengths. Therefore, a significant fraction of photons emitted by the stars in this wavelength range can escape without being scattered or absorbed by dust. Thus, unlike Ly α , the IRAC-1 image is more compact, and it concentrate on the high density peak of stars. We note that the infrared fluxes are higher than those of the LAE sample at $z = 3.1$ by Gronwall et al. (2007), but comparable with those of the IRAC-detected LAEs in Lai et al. (2008). This may be due to high SFR in these galaxies.

The NIR wavelength shown here is similar to the F356W filter of the next generation telescope, the *James Webb Space Telescope* (JWST). The detection limit of the filter in AB magnitude can achieve $m_{\text{AB}} = 28.1$ with 1 hour exposure time (e.g., Zackrisson et al. 2011). Our calcu-

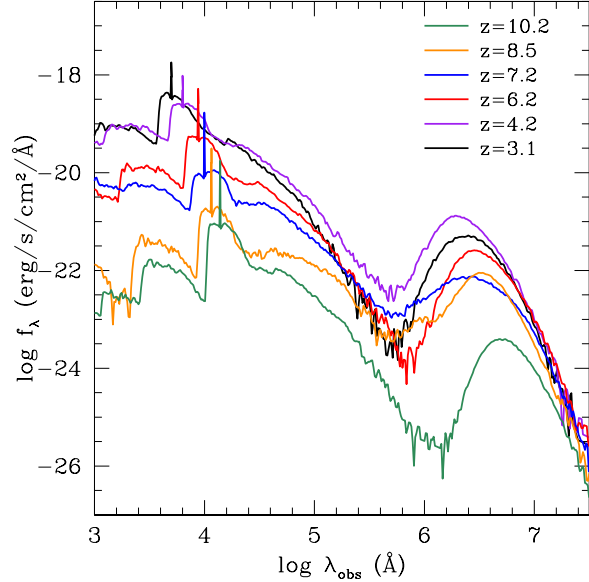


Figure 10. Spectral energy distribution of model galaxies at redshifts $z = 10.2$ (green), 8.5 (orange), 7.2 (blue), 6.2 (purple), and 3.1 (black), respectively.

lations show that the model galaxies have $m_{\text{AB}} = 24.3$ ($z = 3.1$), 25.1 ($z = 6.2$), 28.5 ($z = 8.5$), and 29.8 ($z = 10.2$) at this wavelength. Hence, the JWST will be able to detect the infrared emission from galaxies such as the progenitor of the Milky Way at $z \sim 6$ with a ~ 1 minute exposure time. Even at higher redshifts, these galaxies may be detected with an integration of ~ 2 hours for $z = 8.5$, and ~ 23 hours for $z = 10.2$.

3.2.2 Evolution of Spectral Energy Distribution

The corresponding multi-wavelength SEDs of the most massive galaxy at selected redshift are shown in Figure 10. The shape of the SED changes significantly from $z = 10.2$ to $z = 3.1$, as a result of changes in radiation from stars, absorption of ionizing photons by gas and dust, and re-emission by dust in the infrared. The Ly α line appears to be strong in all cases. The deep decline of UV continuum at $z > 8$ is caused by strong absorption of ionizing photons by the dense gas. Galaxy at lower redshift has a higher floor of continuum emission from stars and accreting BHs, a higher ionization fraction of the gas, and a higher infrared bump owing to increasing amount of dust and absorption. Moreover, due to the effect of negative k-correction, the flux at $\gtrsim 500 \mu\text{m}$ stays close in different redshifts. Our calculations show that the model galaxies have a flux of $f_\nu = 0.043$ ($z = 3.1$), 0.057 ($z = 6.2$), 0.02 ($z = 8.5$), and 0.004 ($z = 10.2$) mJy at $850 \mu\text{m}$ in observed frame. The new radio telescope, *Atacama Large Millimeter/submillimeter Array* (ALMA) may be able to detect such galaxies at $z \sim 6$ with ~ 2 hours integration, and at $z \sim 8.5$ for ~ 20 hours with 16 antennas. Even with ALMA, it may be very difficult to detect such a galaxy at $z = 10.2$ (more than 70 days integration).

From the SEDs, it is interesting to compare the emer-

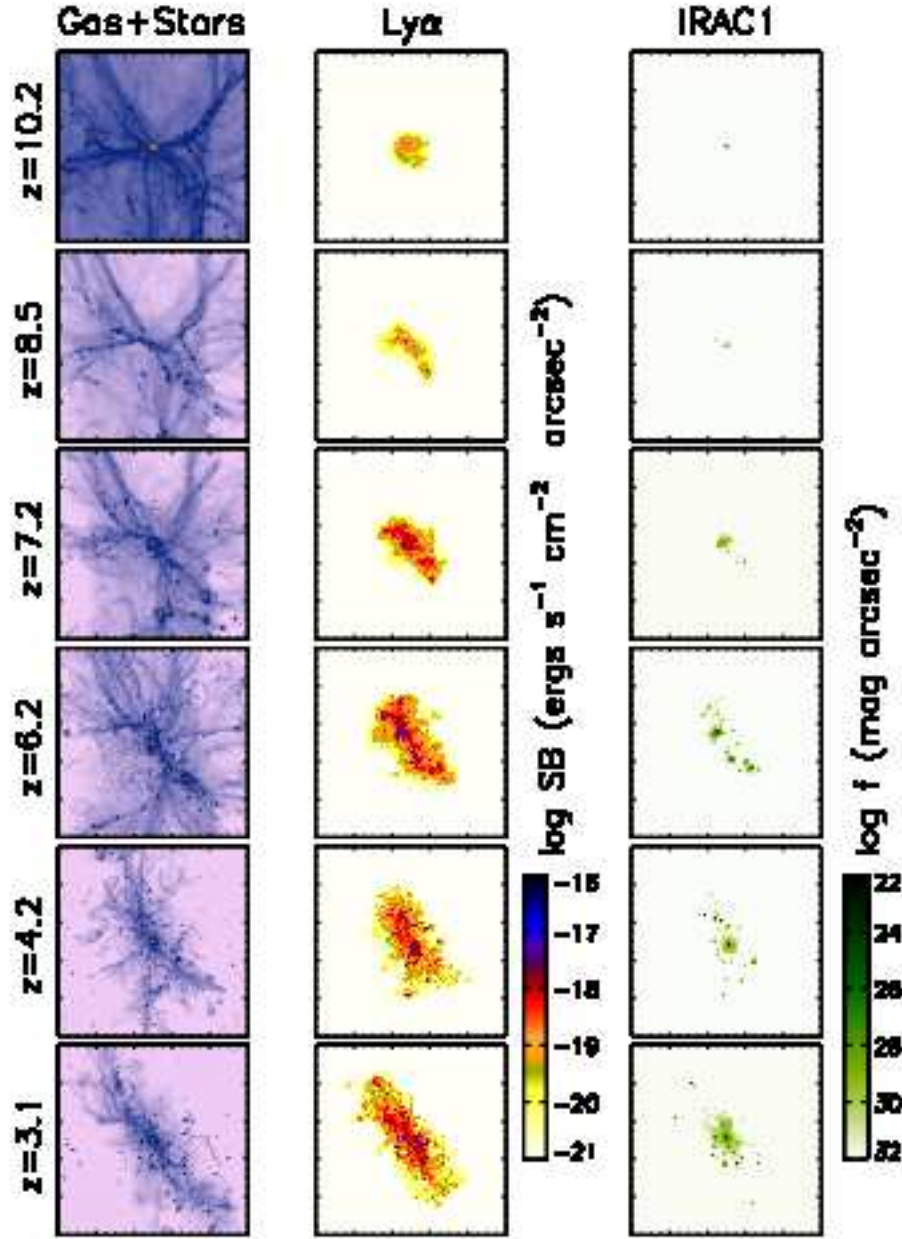


Figure 9. Evolution of galaxies in different wavebands. The left panels show the distribution of gas and stars from the cosmological simulation. Middle panels show the surface brightness of Ly α , and right panels are the flux images in near infrared IRAC-1 ($3.6 \mu\text{m}$) on board of *Spitzer* telescope. The box size is 1 Mpc in comoving scale. Note the middle and right panels show only images of the most massive galaxies corresponding to the redshifts labeled in the left column.

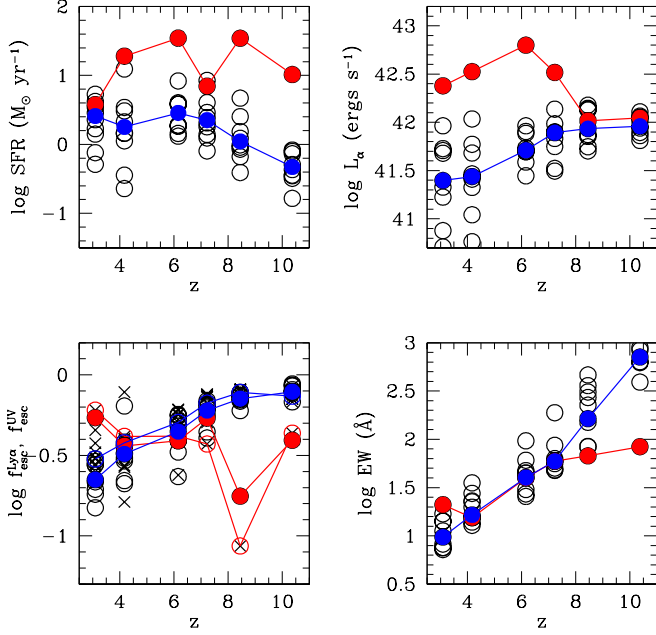


Figure 11. $\text{Ly}\alpha$ properties of modeled galaxies at different redshifts, in clock wise direction: star formation rate, emergent $\text{Ly}\alpha$ luminosity, equivalent width of $\text{Ly}\alpha$ line in rest frame, and photon escape fraction of $\text{Ly}\alpha$ (open circles) and UV continuum (1300 – 1600 Å, crosses). Red and Blue filled circles are the values of the most massive galaxies and the median in our sample at each snapshot, respectively. Filled and open red circles in the panel of escape fraction shows the $\text{Ly}\alpha$ and UV continuum escape fraction of the most massive galaxies, filled and open blue circles are the median values of $\text{Ly}\alpha$ and UV continuum, respectively.

gent $\text{Ly}\alpha$ luminosity and that of the infrared integrated from 8 to 1000 μm in the rest frame. A simple relation between infrared and $\text{Ly}\alpha$ luminosity has been suggested by Kennicutt (1998) through star formation, namely $\text{SFR}(\text{M}_{\odot} \text{ yr}^{-1}) = 4.5 \times 10^{-44} L_{\text{IR}}(\text{ergs s}^{-1})$ and $\text{SFR}(\text{M}_{\odot} \text{ yr}^{-1}) = 0.91 \times 10^{-42} L_{\alpha}(\text{ergs s}^{-1})$ with the assumption of $L_{\alpha}/L_{\text{H}\alpha} = 8.7$ (case B). However, our calculation suggests a more complex relation between $\text{Ly}\alpha$ and infrared luminosity, as inferred from Figure 10. This is because L_{α} depends on $f_{\text{esc}}^{\text{Ly}\alpha}$, while the L_{IR} depends on $f_{\text{esc}}^{\text{UV}}$, and the two escape fractions differ from each other. In our simulations, the $f_{\text{esc}}^{\text{UV}}$ mostly decreases with redshift, and is below 0.5 at $z \lesssim 6$. Hence, the UV continuum may serve as a good tracer of SFR at $z \gtrsim 6$, while $z \lesssim 6$ the infrared flux may be one. In addition, since the modeled galaxies at $z \lesssim 6$ show a smaller value of $f_{\text{esc}}^{\text{Ly}\alpha}$ than 0.5 (see next subsection), hence $\text{Ly}\alpha$ flux also may not be a good indicator of SFR.

3.2.3 The $\text{Ly}\alpha$ Properties

The derived properties of $\text{Ly}\alpha$ emission from these modeled galaxies are shown in Figure 11, in comparison with their corresponding SFR. The most massive galaxies at very high redshift ($z > 6$) maintain a high SFR of $\sim 10 - 30 \text{ M}_{\odot} \text{ yr}^{-1}$ fueled by accretion of cold gas and merging process. The SFR decreases to $\sim 3 \text{ M}_{\odot} \text{ yr}^{-1}$ at $z \sim 3$ owing to depletion

of star-forming gas and suppression by radiation feedback from both stars and accreting BHs. The resulting emergent $\text{Ly}\alpha$ luminosity from recombination of ionizing photons and from excitation cooling increases from $\sim 1.0 \times 10^{42} \text{ ergs s}^{-1}$ at $z = 8.5$ to $\sim 2.3 \times 10^{42} \text{ ergs s}^{-1}$ at $z = 3.1$. The observed LAE luminosity functions show a characteristic luminosity $L_{\text{Ly}\alpha}^* \sim 4.4 \times 10^{42} \text{ ergs s}^{-1}$ at $z = 6.6$ (Ouchi et al. 2010), and $L_{\text{Ly}\alpha}^* \sim 6 \times 10^{42} \text{ ergs s}^{-1}$ at $z = 3.1$ (Ouchi et al. 2008; Gronwall et al. 2007; Blanc et al. 2011), which are comparable to the luminosity range of our modeled galaxies. The median values of SFR moderately decrease with increasing redshift, and show $\sim 0.5 - 3 \text{ M}_{\odot} \text{ yr}^{-1}$. However, the L_{α} does not decrease largely by the redshift evolution of f_{esc} . In addition, a few galaxies in each snapshot are $\text{Ly}\alpha$ bright, and have $\text{Ly}\alpha$ luminosity of $L_{\alpha} \geq 10^{42} \text{ ergs s}^{-1}$, which is detectable with recent observational studies (e.g., Ouchi et al. 2008).

The lower-left panel of figure 11 shows the photon escape fraction of $\text{Ly}\alpha$, $f_{\text{esc}}^{\text{Ly}\alpha}$ and UV continuum $f_{\text{esc}}^{\text{UV}}$, where $f_{\text{esc}}^{\text{UV}}$ is calculated at $\lambda_{\text{rest}} = 1300 - 1600 \text{ Å}$. Both escape fractions appear to increase with time (decreasing redshift), with $f_{\text{esc}}^{\text{Ly}\alpha} \sim 0.18$ at $z = 8.5$ to ~ 0.5 at $z = 3.1$, while $f_{\text{esc}}^{\text{UV}} \sim 0.09$ at $z = 8.5$ to ~ 0.6 at $z = 3.1$. In the early evolution phase, the most massive galaxies are compact and gas-rich. They grow rapidly from accretion of cold gas which fueled intense star formation. The highly concentrated gas and dust efficiently absorb the $\text{Ly}\alpha$ and UV photons, and suppress their escape. At a later time, the gas and stars distribute to a more extended region, and a large fraction of gas is converted to stars. Hence, the photon may easily escape from the galaxy, contributing to a higher photon escape fraction.

On the other hand, the median value of f_{esc} of $\text{Ly}\alpha$ and UV increases monotonically with redshift, e.g., $f_{\text{esc}}^{\text{Ly}\alpha} \sim 0.75$ at $z = 8.5$ to ~ 0.29 at $z = 3.1$, while $f_{\text{esc}}^{\text{UV}} \sim 0.81$ at $z = 8.5$ to ~ 0.38 at $z = 3.1$. Such a trend is consistent with observations by Hayes et al. (2011).

Unlike the most massive galaxies, the low-mass ones have lower SFR and lower dust content, the ISM is less dense and less clumpy, and the metallicity is lower. As a result, the escape fractions are higher in small galaxies than the massive ones.

The EW of $\text{Ly}\alpha$ line is defined by the ratio between the $\text{Ly}\alpha$ flux and the UV flux density f_{UV} in rest frame, where the mean flux density of $\lambda = 1300 - 1600 \text{ Å}$ in rest frame is used. In practice, the EW is estimated by $\text{EW} = \text{EW}_{\text{int}} \frac{f_{\text{Ly}\alpha}}{f_{\text{UV}}}$, where EW_{int} is the intrinsic equivalent width. The EW_{int} depends on the stellar SED and the excitation $\text{Ly}\alpha$ cooling: the younger SED (or top-heavy IMF) and the more efficient $\text{Ly}\alpha$ cooling, the higher EW_{int} .

The resulting $\text{Ly}\alpha$ EWs of the most massive galaxies are shown in the lower right panel of Figure 11. Since the photon escape fraction of $\text{Ly}\alpha$ is close to that of the UV continuum, the EW shown is basically EW_{int} . All three modeled galaxies have $\text{EW} > 20 \text{ Å}$, they are therefore classified as LAEs (e.g., Gronwall et al. 2007). The EW evolves gradually with redshift. At $z > 6$, the EWs are high, $\text{EW} \sim 60 \text{ Å}$, owing to strong $\text{Ly}\alpha$ emission from excitation cooling and AGN activity, while at $z = 3.1$, it drops to $\sim 21 \text{ Å}$ as the $\text{Ly}\alpha$ emission is mainly produced by stellar radiation. The median value increases more steeply with redshift, from $\sim 14 \text{ Å}$

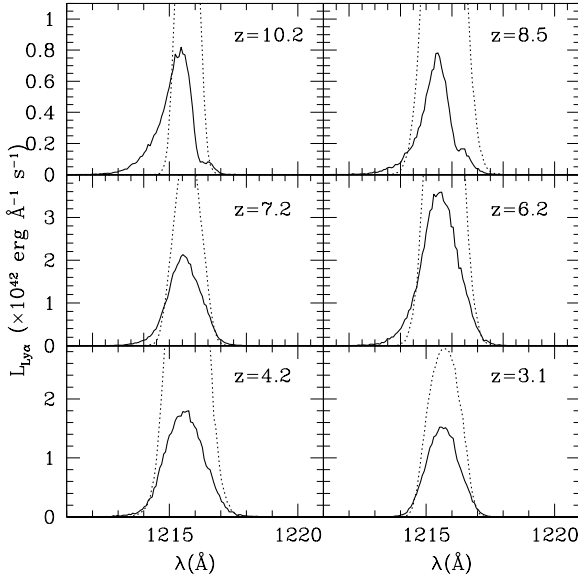


Figure 12. Emergent Ly α profile. Dot and solid lines are the profiles of intrinsically emitted and escaped photons respectively.

at $z = 3.1$ to ~ 164 at $z = 8.5$. These EWs are within the observed range, and the trend is in broad agreement with observations that galaxies at higher redshifts appear to have higher EW than their counterparts at lower redshifts (e.g., Gronwall et al. 2007; Ouchi et al. 2008). Some galaxies at higher redshift $z \gtrsim 8$ show very high EW because the excitation Ly α cooling becomes dominant (Yajima et al. 2011b). However, it will be suppressed significantly by IGM at such a high redshift.

The recent discovery of the most distant LAE, UDFy-38135539, at $z = 8.6$ by Lehnert et al. (2010) marks a milestone in observational cosmology that galaxies form less than 600 million years after the Big Bang. The detected Ly α line flux of this object is $\sim 6 \times 10^{-18}$ ergs cm $^{-2}$ s $^{-1}$, which implies a Ly α luminosity of $\sim 5.5 \times 10^{42}$ ergs s $^{-1}$. This is close to that of our galaxy at $z = 8.5$. Our model suggests that this LAE may have a total mass of $\sim 10^{10-11} M_{\odot}$, a stellar mass of $\sim 10^9 M_{\odot}$, a SFR of the order of $10 M_{\odot}$ yr $^{-1}$, and $f_{\text{esc}}^{\text{Ly}\alpha} \sim 0.18$. We note that Dayal et al. (2011) suggested a lower SFR of $2.7 - 3.7 M_{\odot}$ yr $^{-1}$ for this galaxy by assuming a Ly α escape fraction of 100 per cent. However, our detailed RT calculations show that the escape fraction is much smaller than unity, which means it would require a higher SFR in order to produce the observed Ly α flux.

3.2.4 The Ly α Line Profiles

Figure 12 shows the profiles of Ly α line of the modeled galaxies. The frequency of the intrinsic Ly α photon is sampled from a Maxwellian distribution with the gas temperature at the emission location in the rest frame of the gas. We collect all escaped Ly α photons and estimate the line profile. In practice, the inhomogeneous gas structure can cause the change of flux depending on the viewing angle. Although the Ly α flux can change by some factors (Yajima et al. 2011b), we focus on only the mean value in this paper.

The Ly α lines of our galaxies show mostly a single peak, a common profile of LAEs at high redshifts (e.g., Ouchi et al. 2010). In a static and optically thick medium, the profile can be double peaked, but when the effective optical depth is small due to high relative gas speed or ionization state, there might be only a single peak (Zheng & Miralda-Escudé 2002). In our case, the flow speed of gas is up to ~ 300 km s $^{-1}$, and the gas is highly ionized by stellar and AGN radiation, which result in a single peak.

In addition, the profile at higher redshift shifts to shorter wavelength, and it shows the characteristic shape of gas inflow (Zheng & Miralda-Escudé 2002). Although our simulation includes feedback of stellar wind similar to that of Springel et al. (2005b), the Ly α line profile indicates gas inflow or symmetric in these galaxies. Our result suggests that high-redshift star-forming galaxies may be fueled by efficient inflow of cold gas from the filaments. We will address this issue in detail in a forthcoming paper (Yajima et al. in preparation).

We note that there is a number of studies on inflow and outflow in Ly α lines, both observationally (Kunth et al. 1998) and theoretically (e.g., Verhamme et al. 2006; Dijkstra & Wyithe 2010; Dijkstra, Mesinger, & Wyithe 2011; Barnes et al. 2011). It has been suggested that the IGM correction of Ly α emission may be enhanced due to inflow (e.g., Dijkstra, Lidz, & Wyithe 2007) or decreased via outflows (e.g., Verhamme et al. 2006). However, there is a large uncertainty in the prescription of wind feedback in current simulations. To investigate the velocity field of ISM in high-redshift galaxies, one needs simulations with a realistic wind model and a high spatial resolution comparable to that of line observations, which are currently unavailable and are beyond the scope of this paper. Moreover, we should point out that the line profile can change due to the difference of the sub-grid ISM models.

In addition, the line profile may be highly suppressed and changed by scattering in the intergalactic medium (IGM) (e.g., Santos 2004; Dijkstra et al. 2007; Zheng et al. 2010; Laursen, Sommer-Larsen, & Razoumov 2011). The IGM effectively absorbs the Ly α photons at the line center and at shorter wavelengths by the Hubble flow (e.g., Laursen et al. 2011). Therefore, the inflow feature in our profiles may be disappeared and the shape may change to an asymmetric single peak with only photons at red wing. We will investigate the IGM correction in future work that includes propagation and scattering of Ly α and ionizing photons in the IGM.

3.2.5 The Properties of Ionizing Photons

Figure 13 shows the escape fraction of ionizing photons, $f_{\text{esc}}^{\text{Ion}}$, and the resulting emissivity from both stars and AGNs of the modeled galaxies. The escape fraction of the most massive galaxies has a range of $f_{\text{esc}}^{\text{Ion}} \sim 0.03 - 0.37$, consistent with the results of Dijkstra et al. (2011); Yajima et al. (2011a). In addition, $f_{\text{esc}}^{\text{Ion}}$ decreases with increasing redshift. Unlike the Ly α and non-ionizing UV photons, the ionizing photons can be absorbed by hydrogen gas and dust. At high redshift, the star formation efficiency is small, so a large fraction of hydrogen gas remains neutral and prevent the escape of ionizing photons. The median values do not decrease with redshift due to lower dust mass.

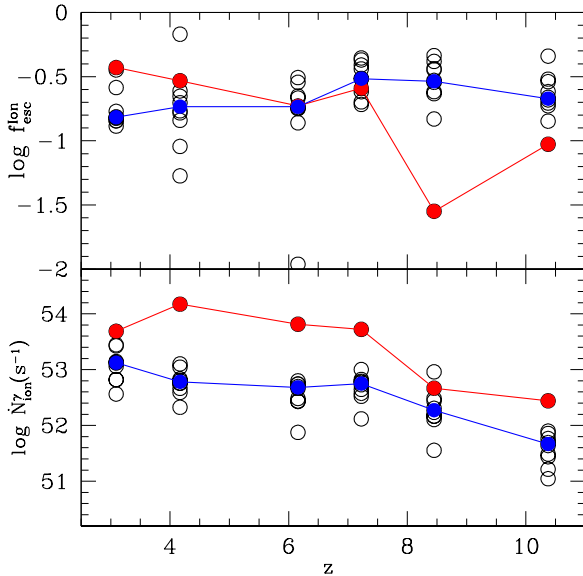


Figure 13. The escape fraction of ionizing photons (top panel) and the resulting emissivity (bottom panel) of modeled galaxies at redshifts $z = 3.1 - 10.2$. Red and Blue filled circles are the values of the most massive galaxies and the median in our sample at each snapshot, respectively.

The emissivity of the ionizing photons roughly increase with decreasing redshift, reaching $\sim 5 \times 10^{53} \text{ s}^{-1}$ at $z = 3.1$. In this work, we do not calculate the RT in the IGM, but the size of the HII bubble around the galaxy may be estimated by a modified Strömgren sphere. Assuming a clumpiness factor of $C = 5$ (Iliev et al. 2007; Pawlik, Schaye, & van Scherpenzeel 2009), the radius of the HII bubble is estimated to be $r = 554, 198, 47$ and 28 kpc at $z = 3.1, 6.2, 8.5$ and 10.2 , respectively. The Ly α photons may pass through the HII bubbles, resulting in a correlation between high-redshift LAEs and HII regions, as suggested by McQuinn et al. (2007). In addition, the median value of ionizing-photons emissivity is smaller due to lower SFR, and hence the HII bubble becomes smaller than that of the most massive galaxy by a factor of $\sim 2 - 6$.

4 DISCUSSION

In observations of Ly α emission from high-redshift galaxies, there are a number of uncertainties regarding the contributions from AGNs (e.g., Wang et al. 2004; Ouchi et al. 2008; Nilsson & Möller 2011), stars, and excitation cooling from cold accretion. With our model, we can separate the radiation components and disentangle the contribution from different sources. Also, in numerical simulations, resolution plays an important role in the robustness of the results. So we discuss these physical and numerical effects on Ly α emission in this Section.

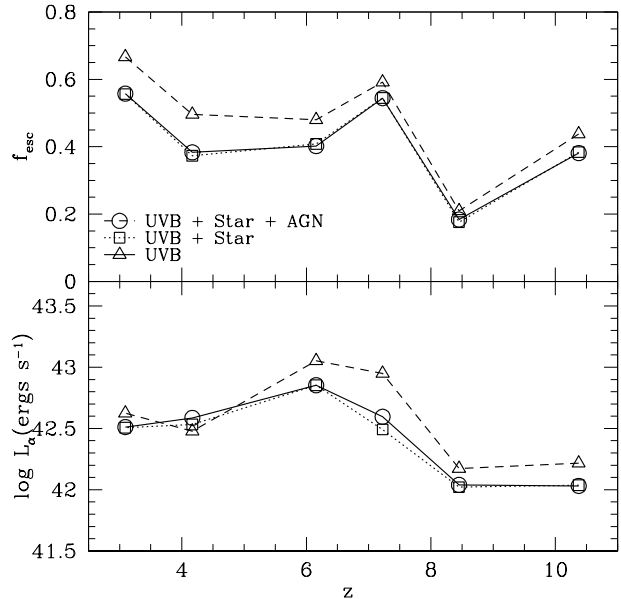


Figure 14. Effects of AGN on escape fraction of Ly α photons (top panel) and the emergent luminosity (bottom panel). The ionization and Ly α luminosity are estimated with radiation from the following sources: UVB only (triangles), UVB + star (squares), and UVB + AGN + star (circles).

4.1 Effects of AGN and Stellar Radiation on Ly α Emission

The effects of AGN and stars on the Ly α emission is shown in Figure 14. It appears that the presence of AGN does not change significantly the Ly α escape fraction. It is because AGNs are usually located in galactic center where the gas density peaks, most of the ionizing photons near Lyman-limit (~ 13.6 eV) are trapped there (e.g., Nagamine et al. 2010; Yajima et al. 2011a) and cannot escape. On the other hand, a fraction of high energy photons can escape from the galaxy without ionizing interstellar gas due to small cross section of gas and dust. Therefore, AGN radiation has little effect on the f_{esc} of Ly α photons. There is no change in f_{esc} in the case where there is no stellar and AGN radiation.

In addition, the AGN does not affect the Ly α luminosity, as shown in the bottom panel of Figure 14. This may be because the BHs in these galaxies are still quite small and the accretion rates are quite low. On the other hand, the presence of stars appears to change the escape fraction and emergent luminosity of Ly α , because the stellar radiation is much stronger than that of AGN in the model galaxies, and the effect becomes stronger at lower redshift. Because Ly α emissivity is produced by the recombination of ionizing photons and collisional excitation from hydrogen gas, the interplay between these two mechanisms determines the outcome. At redshifts $z > 6$, excitation cooling from cold accretion of dense gas becomes comparable to recombination cooling, while at $z \sim 3$, the number of Ly α photons by recombination in HII regions by stars and AGNs outnumbers that from excitation cooling. Therefore, the contribution from stars to the Ly α emission changes with cosmic time and environment. The Ly α emissivity from excitation

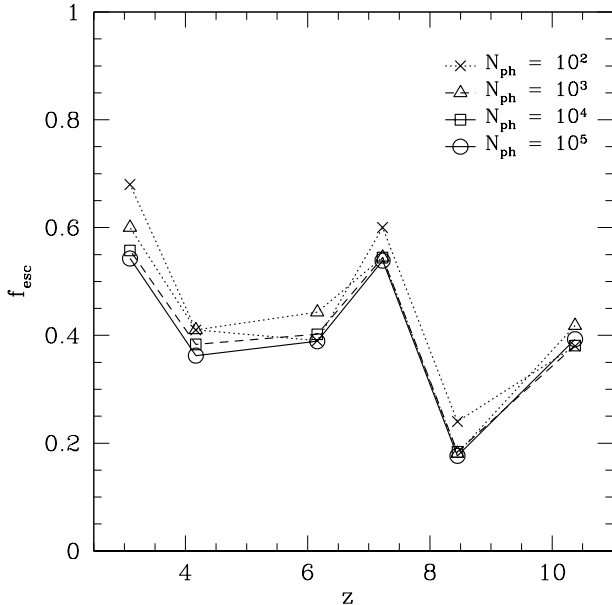


Figure 15. Effects of photon number on the escape fraction of Ly α photons. Open triangles, squares and circles indicate photon packet number $N_{\text{ph}} = 10^2, 10^3, 10^4$, and 10^5 , respectively. The fiducial number used in our general RT calculations is $N_{\text{ph}} = 10^5$.

cooling can be reduced due to the stellar ionization (e.g., Faucher-Giguère et al. 2010). Moreover, the distribution of excitation Ly α cooling can be more extended than star-forming regions, resulting in higher escape fraction. Thus, the escape fraction and emergent luminosity of Ly α somewhat increase in the case without stellar radiation.

4.2 Resolution Effect

Figure 15 demonstrates effects of photon number on the escape fraction of Ly α photons, with different number of photon packets, $N_{\text{ph}} = 10^2, 10^3, 10^4$ and 10^5 . It appears that the results converge once the photon number is above 10^4 , which is an order of magnitude lower than the fiducial $N_{\text{ph}} = 10^5$ in our general RT calculations. The relative difference between $N_{\text{ph}} = 10^4$ and 10^5 is 1-6 per cent. Of course, the photon number should increase with galaxy mass, but for our modeled galaxies, $N_{\text{ph}} = 10^5$ should be sufficient.

The effects of grid resolution on the escape fraction of Ly α photons is presented in Figure 16, where results from different maximum refinement level (RL) are compared. It appears that f_{esc} changes dramatically with RL, but it converges at $\text{RL} \geq 10$. Grids with poor resolution can produce artificially high f_{esc} by a factor of more than 20. Because most of the Ly α photons are created in high-density gas clumps, where they are also effectively absorbed by numerous scatterings, sufficiently resolving the gas density field is important in the calculation of Ly α RT. If we follow the resolution of $\text{RL} = 10$ with uniform grids, it would require a number of cells of $\sim 2048^3$, too expensive for RT simulations with the current computational facility. In fact, the current limit is $\sim 500^3$, as demonstrated by recent work on three-dimensional RT calculations using uniform grid (e.g.,

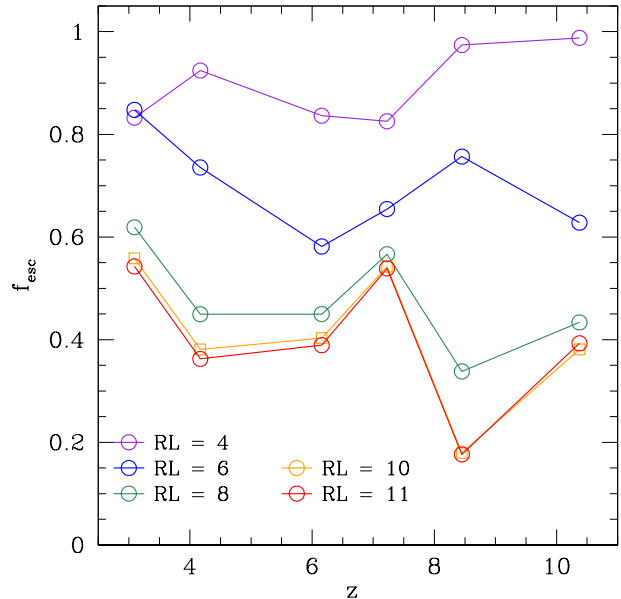


Figure 16. Effect of grid resolution on the escape fraction of Ly α photons. Different color indicates different maximum refinement level (RL): purple – $\text{RL} = 4$, blue – $\text{RL} = 6$, green – $\text{RL} = 8$, orange – $\text{RL} = 10$, and red – $\text{RL} = 11$. The fiducial RL used in our general RT calculations is 11. The cell size of the highest refinement level is $1/2^{\text{RL}+1}$ Mpc in comoving scale.

Iliev et al. 2007; Yajima et al. 2011a). Therefore, adaptive refinement grid is critical in the RT calculation of Ly α emission.

5 SUMMARY

We have presented an improved, three-dimensional, Monte Carlo radiative transfer code ART² to study multi-wavelength properties of galaxies. It has the following essential features:

- It couples Ly α line, ionization of neutral hydrogen, and multi-wavelength continuum radiative transfer. The Ly α module includes emission from both recombination and collisional excitation, and the continuum includes emission from X-ray to radio.
- It employs an adaptive grid scheme in 3-D Cartesian coordinates, which handles an arbitrary geometry and covers a large dynamic range over several orders of magnitude. Such a grid is critical in resolving the clumpy, highly inhomogeneous density field in the RT calculations.
- It adopts a two-phase ISM model in which the cold, dense clouds are embedded in a hot, diffuse medium in pressure equilibrium. In the case where hydrodynamic simulations have sufficient resolution to resolve the multi-phase ISM, this model ensures an appropriate prescription of the ISM physics, which is important for studying dust properties in galaxies.
- It includes a supernova-origin dust model in which the dust is produced by Type-II supernovae, which is especially relevant for dust in high-redshift, young objects, because

there are insufficient low-mass, old AGB stars in these systems to produce the observed amount of dust from the classical dust models.

- It follows the radiation from stars and AGNs, and calculates the scattering, absorption, and re-emission of the surrounding medium. It efficiently and self-consistently produces SEDs and images in a full spectrum, including Ly α emission line and continuum from X-ray to millimeter, as well as ionization structures of the medium, for direct comparison with multi-band observations.

- It can be easily applied to either grid- or particle-based hydrodynamical simulations and has broad applications in cosmology.

We have tested the new ART² extensively, and found that the coupling of Ly α line and continuum enables a self-consistent and accurate calculation of the Ly α properties of galaxies, as the equivalent width of the Ly α line depends on the UV continuum, and the escape fraction of Ly α photons strongly depends on the ionization structure and the dust content of the object.

We applied the code to a cosmological SPH simulation of a Milky Way-like galaxy, and studied in details a sample of massive galaxies at redshift $z=3.1$ - 10.2 . We find that most of these galaxies are Ly α emitters. The escape fraction of Ly α photons of the most massive galaxy in each snap shot increases with decreasing redshift, from about 0.18 at redshift $z \sim 8.5$ to 0.6 at $z \sim 3$. The emergent Ly α luminosity shows similar trend, increasing from $L_\alpha = 1.0 \times 10^{42}$ ergs s⁻¹ at $z \sim 8.5$ to $L_\alpha = 2.3 \times 10^{42}$ ergs s⁻¹ at $z \sim 3$. The equivalent widths of these galaxies change with redshift as well, from ~ 67 Å at $z \sim 8.5$ to ~ 21 Å at $z \sim 3$. The profiles of the resulting Ly α lines commonly show single peak, and the peak of the profile at $z \gtrsim 6$ is shifted to shorter wavelength, implying gas inflow from surrounding filaments. On the other hand, the median values in our galaxy sample shows somewhat different trend from that of the most massive ones. The escape fraction monotonically increases with redshift, while the Ly α luminosity shows a weak evolution, as a result of the interplay between SFR and escape fraction.

Our results suggest that the LAEs and their properties evolve with cosmic time, and that the first LAEs in the early universe, such as currently the most distant one detected at $z \sim 8.6$ (Lehnert et al. 2010), may be dwarf galaxies with a total mass of $\sim 10^{10-11} M_\odot$ fueled by cold gas accretion. They may have a star formation rate of order of $10 M_\odot$ yr⁻¹, and a Ly α escape fraction of ~ 20 per cent.

ACKNOWLEDGMENTS

We thank Mark Dijkstra, Claude-André Faucher-Giguère, Caryl Gronwall, Robin Ciardullo, Lars Hernquist, and Avi Loeb for stimulating discussions and helpful comments, as well as the referee for an insightful and constructive report which has helped improve the manuscript significantly. Support from NSF grants AST-0965694, AST-1009867 (to YL), and AST-0807075 (to TA) is gratefully acknowledged. YL thanks the Institute for Theory and Computation (ITC) at Harvard University where the project was started for warm hospitality. We acknowledge the Research Computing and Cyberinfrastructure unit of Information Technology Services at The Pennsylvania State University for pro-

viding computational resources and services that have contributed to the research results reported in this paper (URL: <http://rcc.its.psu.edu>). The Institute for Gravitation and the Cosmos is supported by the Eberly College of Science and the Office of the Senior Vice President for Research at the Pennsylvania State University.

REFERENCES

- Abel T., Norman M. L., Madau P., 1999, *ApJ*, 523, 66
 Abel T., Wandelt B. D., 2002, *MNRAS*, 330, L53
 Adams T. F., 1972, *ApJ*, 174, 439
 Ahn S., Lee H., Lee H. M., 2000, *Journal of Korean Astronomical Society*, 33, 29
 Ahn S.-H., Lee H.-W., Lee H. M., 2001, *ApJ*, 554, 604
 —, 2002, *ApJ*, 567, 922
 Andre P., Ward-Thompson D., Motte F., 1996, *A&A*, 314, 625
 Auer L. H., 1968, *ApJ*, 153, 783
 Avery L. W., House L. L., 1968, *ApJ*, 152, 493
 Baek S., Di Matteo P., Semelin B., Combes F., Revaz Y., 2009, *A&A*, 495, 389
 Barnes J., Hut P., 1986, *Nature*, 324, 446
 Barnes L. A., Haehnelt M. G., Tescari E., Viel M., 2011, *ArXiv* 1101.3319
 Bianchi S., Davies J. I., Alton P. B., 2000, *A&A*, 359, 65
 Bjorkman J. E., Wood K., 2001, *ApJ*, 554, 615
 Blanc G. A., et al., 2011, *ApJ*, 736, 31
 Blitz L., Rosolowsky E., 2006, *ApJ*, 650, 933
 Bondi H., 1952, *MNRAS*, 112, 195
 Bondi H., Hoyle F., 1944, *MNRAS*, 104, 273
 Bruzual G., Charlot S., 2003, *MNRAS*, 344, 1000
 Cen R., 1992, *ApJS*, 78, 341
 Chakrabarti S., Whitney B. A., 2009, *ApJ*, 690, 1432
 Ciardi B., Ferrara A., Marri S., Raimondo G., 2001, *MNRAS*, 324, 381
 Code A. D., Whitney B. A., 1995, *ApJ*, 441, 400
 Cowie L. L., Hu E. M., 1998, *AJ*, 115, 1319
 Cuby J.-G., Hibon P., Lidman C., Le Fèvre O., Gilmozzi R., Moorwood A., van der Werf P., 2007, *A&A*, 461, 911
 Dame T. M., Elmegreen B. G., Cohen R. S., Thaddeus P., 1986, *ApJ*, 305, 892
 Davé R., Hernquist L., Katz N., Weinberg D. H., 1999, *ApJ*, 511, 521
 Dawson S., et al., 2004, *ApJ*, 617, 707
 Dayal P., Maselli A., Ferrara A., 2011, *MNRAS*, 410, 830
 Di Matteo T., Colberg J., Springel V., Hernquist L., Sijacki D., 2008, *ApJ*, 676, 33

Di Matteo T., Springel V., Hernquist L., 2005, *Nature*, 433, 604

Dijkstra M., Haiman Z., Spaans M., 2006, *ApJ*, 649, 14

Dijkstra M., Lidz A., Wyithe J. S. B., 2007, *MNRAS*, 377, 1175

Dijkstra M., Loeb A., 2008, *MNRAS*, 386, 492

Dijkstra M., Mesinger A., Wyithe J. S. B., 2011, *MNRAS*, 548

- Dijkstra M., Wyithe J. S. B., 2010, MNRAS, 408, 352
- Dolag K., Borgani S., Murante G., Springel V., 2009, MNRAS, 399, 497
- Dwek E., Galliano F., Jones A. P., 2007, ApJ, 662, 927
- Efstathiou A., Rowan-Robinson M., 1990, MNRAS, 245, 275
- Faucher-Giguère C., Kereš D., Dijkstra M., Hernquist L., Zaldarriaga M., 2010, ApJ, 725, 633
- Field G. B., 1959, ApJ, 129, 551
- Finkelstein S. L., et al., 2011, ApJ, 729, 140
- Folini D., Walder R., Psarros M., Desboeufs A., 2003, in Astronomical Society of the Pacific Conference Series, Vol. 288, Stellar Atmosphere Modeling, I. Hubeny, D. Mihalas, & K. Werner, ed., pp. 433–+
- Fuller G. A., Myers P. C., 1992, ApJ, 384, 523
- Fynbo J. P. U., Ledoux C., Möller P., Thomsen B., Burud I., 2003, A&A, 407, 147
- Fynbo J. U., Möller P., Thomsen B., 2001, A&A, 374, 443
- Gawiser E., et al., 2006, ApJ, 642, L13
- Gnedin N. Y., Abel T., 2001, New Astronomy, 6, 437
- Gnedin N. Y., Kravtsov A. V., Chen H. W., 2008, ApJ, 672, 765
- Gnedin N. Y., Ostriker J. P., 1997, ApJ, 486, 581
- Gronwall C., et al., 2007, ApJ, 667, 79
- Haardt F., Madau P., 1996, ApJ, 461, 20
- Hamilton D. R., 1940, Physical Review, 58, 122
- Hansen M., Oh S. P., 2006, MNRAS, 367, 979
- Harries T. J., Monnier J. D., Symington N. H., Kurosawa R., 2004, MNRAS, 350, 565
- Harrington J. P., 1973, MNRAS, 162, 43
- , 1974, MNRAS, 166, 373
- Hasegawa K., Umemura M., 2010, MNRAS, 407, 2632
- Hayes M., et al., 2010, Nature, 464, 562
- Hayes M., Schaerer D., Östlin G., Mas-Hesse J. M., Atek H., Kunth D., 2011, ApJ, 730, 8
- Hernquist L., Katz N., 1989, ApJS, 70, 419
- Hirashita H., Nozawa T., Kozasa T., Ishii T. T., Takeuchi T. T., 2005, MNRAS, 357, 1077
- Hockney R. W., Eastwood J. W., 1981, Computer Simulation Using Particles, Hockney, R. W. & Eastwood, J. W., ed.
- Hopkins P. F., Hernquist L., Cox T. J., Di Matteo T., Robertson B., Springel V., 2006, ApJS, 163, 1
- Horton A., Parry L., Bland-Hawthorn J., Cianci S., King D., McMahon R., Medlen S., 2004, in Society of Photo-Optical Instrumentation Engineers (SPIE) Conference Series, Vol. 5492, Society of Photo-Optical Instrumentation Engineers (SPIE) Conference Series, A. F. M. Moorwood & M. Iye, ed., pp. 1022–1032
- Hoyle F., Lyttleton R. A., 1941, MNRAS, 101, 227
- Hu E. M., Cowie L. L., 2006, Nature, 440, 1145
- Hu E. M., Cowie L. L., Barger A. J., Capak P., Kakazu Y., Trouille L., 2010, ApJ, 725, 394
- Hu E. M., Cowie L. L., Capak P., McMahon R. G., Hayashino T., Komiyama Y., 2004, AJ, 127, 563
- Hu E. M., Cowie L. L., McMahon R. G., 1998, ApJ, 502, L99+
- Hu E. M., Cowie L. L., McMahon R. G., Capak P., Iwamuro F., Kneib J.-P., Maihara T., Motohara K., 2002, ApJ, 568, L75
- Hu E. M., McMahon R. G., 1996, Nature, 382, 231
- Hui L., Gnedin N. Y., 1997, MNRAS, 292, 27
- Hummer D. G., 1962, MNRAS, 125, 21
- Iliev I. T., Mellema G., Shapiro P. R., Pen U., 2007, MNRAS, 376, 534
- Iliev I. T., et al., 2009, MNRAS, 400, 1283
- Iliev I. T., et al., 2006, MNRAS, 371, 1057
- Iye M., et al., 2006, Nature, 443, 186
- Jonsson P., 2006, MNRAS, 372, 2
- Kashikawa N., et al., 2006, ApJ, 648, 7
- Katz N., Weinberg D. H., Hernquist L., Miralda-Escudé J., 1996, ApJ, 457, L57+
- Kennicutt Jr. R. C., 1998, ARA&A, 36, 189
- Kodaira K., et al., 2003, PASJ, 55, L17
- Komatsu E., et al., 2009, ApJS, 180, 330
- Kunth D., Mas-Hesse J. M., Terlevich E., Terlevich R., Lequeux J., Fall S. M., 1998, A&A, 334, 11
- Lai K., Huang J.-S., Fazio G., Cowie L. L., Hu E. M., Kakazu Y., 2007, ApJ, 655, 704
- Lai K., et al., 2008, ApJ, 674, 70
- Larson R. B., 1981, MNRAS, 194, 809
- Laursen P., Razoumov A. O., Sommer-Larsen J., 2009a, ApJ, 696, 853
- Laursen P., Sommer-Larsen J., 2007, ApJ, 657, L69
- Laursen P., Sommer-Larsen J., Andersen A. C., 2009b, ApJ, 704, 1640
- Laursen P., Sommer-Larsen J., Razoumov A. O., 2011, ApJ, 728, 52
- Lefevre J., Bergeat J., Daniel J.-Y., 1982, A&A, 114, 341
- Lefevre J., Daniel J.-Y., Bergeat J., 1983, A&A, 121, 51
- Lehnert M. D., et al., 2010, Nature, 467, 940
- Li Y., et al., 2007, ApJ, 665, 187
- Li Y., et al., 2008, ApJ, 678, 41
- Loeb A., Rybicki G. B., 1999, ApJ, 524, 527
- Lopez B., Mekarnia D., Lefevre J., 1995, A&A, 296, 752
- Lucy L. B., 1999, A&A, 344, 282
- Maier C., et al., 2003, A&A, 402, 79
- Maiolino R., Schneider R., Oliva E., Bianchi S., Ferrara A., Mannucci F., Pedani M., Roca Sogorb M., 2004, Nature, 431, 533
- Malhotra S., Rhoads J. E., 2004, ApJ, 617, L5
- Maselli A., Ferrara A., Ciardi B., 2003, MNRAS, 345, 379
- McKee C. F., Ostriker J. P., 1977, ApJ, 218, 148
- McQuinn M., Hernquist L., Zaldarriaga M., Dutta S., 2007, MNRAS, 381, 75
- Mellema G., Iliev I. T., Alvarez M. A., Shapiro P. R., 2006, New Astronomy, 11, 374
- Nagamine K., Choi J., Yajima H., 2010, ApJ, 725, L219
- Neufeld D. A., 1990, ApJ, 350, 216
- , 1991, ApJ, 370, L85
- Nilsson K. K., Möller P., 2011, A&A, 527, L7+
- Nilsson K. K., et al., 2007, A&A, 471, 71
- Nozawa T., Kozasa T., Umeda H., Maeda K., Nomoto K., 2003, ApJ, 598, 785
- Ono Y., et al., 2010a, MNRAS, 402, 1580
- Ono Y., Ouchi M., Shimasaku K., Dunlop J., Farrah D., McLure R., Okamura S., 2010b, ApJ, 724, 1524
- Osterbrock D. E., 1989, Astrophysics of gaseous nebulae and active galactic nuclei, University Science Books, Mill Valley, CA, ed.

- Osterbrock D. E., Ferland G. J., 2006, *Astrophysics of gaseous nebulae and active galactic nuclei*, Osterbrock, D. E. & Ferland, G. J., ed.
- Ota K., et al., 2008, *ApJ*, 677, 12
- Ouchi M., et al., 2008, *ApJS*, 176, 301
- Ouchi M., et al., 2003, *ApJ*, 582, 60
- Ouchi M., et al., 2010, *ApJ*, 723, 869
- Ouchi M., et al., 2004, *ApJ*, 611, 660
- Partridge R. B., Peebles P. J. E., 1967, *ApJ*, 147, 868
- Pawlik A. H., Schaye J., van Scherpenzeel E., 2009, *MNRAS*, 394, 1812
- Pentericci L., Grazian A., Fontana A., Castellano M., Giallongo E., Salimbeni S., Santini P., 2009, *A&A*, 494, 553
- Pierleoni M., Maselli A., Ciardi B., 2009, *MNRAS*, 393, 872
- Pinte C., Ménard F., Duchêne G., Bastien P., 2006, *A&A*, 459, 797
- Pirzkal N., Malhotra S., Rhoads J. E., Xu C., 2007, *ApJ*, 667, 49
- Press W. H., Teukolsky S. A., Vetterling W. T., Flannery B. P., 1992, *Numerical recipes in FORTRAN. The art of scientific computing*, Press, W. H., Teukolsky, S. A., Vetterling, W. T., & Flannery, B. P., ed.
- Razoumov A. O., Norman M. L., Abel T., Scott D., 2002, *ApJ*, 572, 695
- Razoumov A. O., Sommer-Larsen J., 2010, *ApJ*, 710, 1239
- Rhoads J. E., et al., 2003, *AJ*, 125, 1006
- Rhoads J. E., Malhotra S., Dey A., Stern D., Spinrad H., Jannuzi B. T., 2000, *ApJ*, 545, L85
- Rosolowsky E., 2005, *PASP*, 117, 1403
- , 2007, *ApJ*, 654, 240
- Rowan-Robinson M., 1980, *ApJS*, 44, 403
- Salpeter E. E., 1955, *ApJ*, 121, 161
- Sanders D. B., Scoville N. Z., Solomon P. M., 1985, *ApJ*, 289, 373
- Santos M. R., 2004, *MNRAS*, 349, 1137
- Schaerer D., Hayes M., Verhamme A., Teyssier R., 2011, *ArXiv 1104.5383*
- Schmidt M., 1959, *ApJ*, 129, 243
- Schneider R., Ferrara A., Salvaterra R., 2004, *MNRAS*, 351, 1379
- Scoville N. Z., Yun M. S., Sanders D. B., Clemens D. P., Waller W. H., 1987, *ApJS*, 63, 821
- Semelin B., Combes F., Baek S., 2007, *A&A*, 474, 365
- Shimasaku K., et al., 2006, *PASJ*, 58, 313
- Solomon P. M., Rivolo A. R., Barrett J., Yahil A., 1987, *ApJ*, 319, 730
- Spitzer L., 1978, *Physical processes in the interstellar medium*, Spitzer, L., ed.
- Springel V., 2005, *MNRAS*, 364, 1105
- Springel V., Di Matteo T., Hernquist L., 2005a, *ApJL*, 620, L79
- , 2005b, *MNRAS*, 361, 776
- Springel V., Hernquist L., 2002, *MNRAS*, 333, 649
- , 2003a, *MNRAS*, 339, 289
- , 2003b, *MNRAS*, 339, 312
- Springel V., et al., 2008, *MNRAS*, 391, 1685
- Springel, V. and Yoshida, N. and White, S. D. M., 2001, *New Astronomy*, 6, 79
- Stark D. P., Ellis R. S., Richard J., Kneib J.-P., Smith G. P., Santos M. R., 2007, *ApJ*, 663, 10
- Steidel C. C., Adelberger K. L., Shapley A. E., Pettini M., Dickinson M., Giavalisco M., 2000, *ApJ*, 532, 170
- Steinacker J., Bacmann A., Henning T., 2006, *ApJ*, 645, 920
- Steinacker J., Henning T., Bacmann A., Semenov D., 2003, *A&A*, 401, 405
- Stenflo J. O., 1980, *A&A*, 84, 68
- Stern D., Yost S. A., Eckart M. E., Harrison F. A., Helfand D. J., Djorgovski S. G., Malhotra S., Rhoads J. E., 2005, *ApJ*, 619, 12
- Strömgren B., 1939, *ApJ*, 89, 526
- Susa H., 2006, *PASJ*, 58, 445
- Taniguchi Y., et al., 2005, *PASJ*, 57, 165
- Tasitsiomi A., 2006, *ApJ*, 648, 762
- Todini P., Ferrara A., 2001, *MNRAS*, 325, 726
- Trac H., Gnedin N. Y., 2011, *Advanced Science Letters*, 4, 228
- Umemura M., Nakamoto T., Susa H., 1999, in *Astrophysics and Space Science Library*, Vol. 240, Numerical Astrophysics, S. M. Miyama, K. Tomisaka, & T. Hanawa, ed., pp. 43–+
- Verhamme A., Schaerer D., Maselli A., 2006, *A&A*, 460, 397
- Wadepuhl M., Springel V., 2011, *MNRAS*, 410, 1975
- Wang J. X., et al., 2004, *ApJ*, 608, L21
- Ward-Thompson D., Scott P. F., Hills R. E., Andre P., 1994, *MNRAS*, 268, 276
- Weingartner J. C., Draine B. T., 2001, *ApJ*, 548, 296
- Whitney B. A., Hartmann L., 1992, *ApJ*, 395, 529
- Whitney B. A., Wood K., Bjorkman J. E., Wolff M. J., 2003, *ApJ*, 591, 1049
- Willis J. P., Courbin F., Kneib J.-P., Minniti D., 2008, *MNRAS*, 384, 1039
- Witt A. N., 1977, *ApJS*, 35, 1
- Witt A. N., Thronson Jr. H. A., Capuano Jr. J. M., 1992, *ApJ*, 393, 611
- Wolf S., Henning T., Stecklum B., 1999, *A&A*, 349, 839
- Xu G., 1995, *ApJS*, 98, 355
- Yajima H., Choi J.-H., Nagamine K., 2011a, *MNRAS*, 412, 411
- Yajima H., Li Y., Zhu Q., Abel T., Gronwall C., Ciardullo R., 2011b, *arXiv:1112.1031*
- Yajima H., Umemura M., Mori M., Nakamoto T., 2009, *MNRAS*, 398, 715
- Zackrisson E., Rydberg C., Schaerer D., Ostlin G., Tuli M., 2011, *ArXiv 1105.0921*
- Zheng Z., Cen R., Trac H., Miralda-Escudé J., 2010, *ApJ*, 716, 574
- , 2011, *ApJ*, 726, 38
- Zheng Z., Miralda-Escudé J., 2002, *ApJ*, 578, 33